Single-cell profiling of trabecular meshwork identifies mitochondrial dysfunction in a glaucoma model that is protected by vitamin B3 treatment

Nicholas Tolman[1,2 *]
Taibo Li[3, *]
Revathi Balasubramanian[1 *]
Guorong Li[4]
Violet Bupp-Chickering[1]
Ruth A. Kelly[4]
Marina Simón[1]
John Peregrin[1]
Christa Montgomery[1]
W. Daniel Stamer[4 #]
Jiang Qian[5 #]
Simon W.M. John[1,6 #]

*Co-first authors
[#]Corresponding authors

1. Department of Ophthalmology, Columbia University Irving Medical Center, New York, NY

2. Graduate School of Biomedical Sciences, Tufts University School of Medicine, Boston, MA

3. Department of Biomedical Engineering, Johns Hopkins University, Baltimore, MD

4. Department of Ophthalmology, Duke University, Durham, NC 27710.

5. Department of Ophthalmology, Johns Hopkins School of Medicine, Baltimore, MD

6. Zuckerman Mind Brain Behavior Institute, Columbia University, New York, NY

Keywords: intraocular pressure, glaucoma, trabecular meshwork, LMX1B, mitochondrial dysfunction, nicotinamide, vitamin B, metabolism, bioenergetic support, resilience, single cell, single nucleus, RNA sequencing, ATAC sequencing, multiome

Abstract:

Since the trabecular meshwork (TM) is central to intraocular pressure (IOP) regulation and glaucoma, a deeper understanding of its genomic landscape is needed. We present a multimodal, single-cell resolution analysis of mouse limbal cells (includes TM). In total, we sequenced 9,394 wild-type TM cell transcriptomes. We discovered three TM cell subtypes with characteristic signature genes validated by immunofluorescence on tissue sections and whole-mounts. The subtypes are robust, being detected in datasets for two diverse mouse strains and in independent data from two institutions. Results show compartmentalized enrichment of critical pathways in specific TM cell subtypes. Distinctive signatures include increased expression of genes responsible for 1) extracellular matrix structure and metabolism (TM1 subtype), 2) secreted ligand signaling to support Schlemm's canal cells (TM2), and 3) contractile and mitochondrial/metabolic activity (TM3). ATAC-sequencing data identified active transcription factors in TM cells, including LMX1B. Mutations in *LMX1B* cause high IOP and glaucoma. LMX1B is emerging as a key transcription factor for normal mitochondrial function and its expression is much higher in TM3 cells than other limbal cells. To understand the role of LMX1B in TM function and glaucoma, we single-cell sequenced limbal cells from $Lmx1b^{V265D/+}$ mutant mice. In *V265D/+* mice, TM3 cells were uniquely affected by pronounced mitochondrial pathway changes. This supports a primary role of mitochondrial dysfunction within TM3 cells in initiating the IOP elevation that causes glaucoma in these mice. Importantly, treatment with vitamin B_3 (nicotinamide), to enhance mitochondrial function and metabolic resilience, significantly protected *Lmx1b* mutant mice from IOP elevation.

Introduction:

Aqueous humor (AH) dynamics and pressure homeostasis are important for proper ocular inflation and vision. Elevated intraocular pressure (IOP) is a key risk factor for glaucoma, a serious blinding disorder that affects 80 million people worldwide (Quigley and Broman, 2006). IOP is controlled by continually adjusting resistance to drainage (outflow) of AH through the trabecular meshwork (TM) and Schlemm's canal (SC), the primary route of AH outflow from the eye. AH percolates through the TM before exiting the eye through SC and then entering the venous circulation. As the most abundant constituent of the conventional outflow pathway, TM cells are central in regulating AH drainage and IOP. Despite significant advances over the past few decades, a much deeper understanding of the molecular mechanisms governing TM cell health and function, as well as the pathological alterations responsible for increased outflow resistance, elevated IOP, and increased glaucoma risk are still needed.

The TM is located at the inner aspect of the wall of the eye at the iridocorneal angle just anterior to where the iris and cornea meet (i.e. the limbus). In humans, the TM is morphologically separated into distinct zones, including the uveal, corneoscleral, and juxtacanalicular trabecular meshwork (JCT), which lies adjacent to the SC. AH first drains through the uveal and corneoscleral meshwork whose TM cells have endothelial-like properties (Buffault et al., 2020; Keller and Peters, 2022; Stamer and Clark, 2017). In these regions, the TM consists of beams and plates made of various extracellular matrix (ECM) components including fibrillar collagens (Abu-Hassan et al., 2014; Acott and Kelley, 2008; Fuchshofer et al., 2006; Vittal et al., 2005; Yue, 1996). The beams and plates are covered with monolayers of TM cells. AH drains through a tortuous series of intertrabecular spaces, which run between the beams, ensuring interaction with TM cells. Next, AH flows into the less structured JCT region before entering the SC. The JCT consists of TM cells that are fibroblast-like extending their processes onto neighboring JCT and SC cells. JCT TM cells are embedded within a diffuse ECM ground substance (including glycosaminoglycans, Johnson, 2006; Keller and Acott, 2013; Stamer and Clark, 2017; Vranka et al., 2015) and have contractile smooth muscle-like properties (Stamer and Clark, 2017; Tian et al., 2009). Importantly, cells in the JCT region impose critical resistance to AH outflow with a major site of resistance to outflow being located in the tissue where the JCT and SC meet (Acott and Kelley, 2008; Johnson, 2006; Overby et al., 2009; Tamm, 2009).

Regulation of AH outflow resistance and IOP homeostasis by TM cells is complicated. AH outflow is modulated by: 1) The physical properties (shape/volume and contractility) of the TM cells. For example, some TM cells have smooth muscle-like properties that adjust outflow resistance and thus IOP by controlling cellular contractility (Rao et al., 2005; Syriani et al., 2009; Thieme et al., 2000; Tian and Kaufman, 2005; Zhang and Rao, 2005, Rao et al., 2001; Wang et al., 2018; Yu et al., 2008). 2) The effects of different TM cell types on both the composition and abundance of ECM in the JCT due to ECM synthesis/ metabolism and phagocytic activity. 3) The paracrine or physical effects of TM cells on SC and possibly the vasculature just distal to SC (Balasubramanian et al., 2024; Kizhatil et al., 2014; Stamer and Acott, 2012; Thomson et al., 2021).

Due to their importance, a more detailed molecular characterization of TM cells is still required. The degree to which specific pathways and modulatory roles are compartmentalized or shared by specific TM cell subtypes and how specific subtypes influence each other and the SC are not known. In fact, the number of molecularly distinct subtypes is currently unknown as is the role of the > 120 genes associated with elevated IOP within these subtypes (Gharahkhani et al., 2021). Although the TM has fewer beams and a narrower drainage path in mice, developmental, functional and anatomical similarities between human and mouse TM make mice a valuable model for studying the molecular characteristics, heterogeneity, subtypes and distribution of TM cells (Chen et al., 2016; Smith et al., 2001).

Single-cell resolution transcriptomic profiling is revolutionizing the molecular characterization of cell types and cellular heterogeneity (single-cell RNA sequencing, scRNA-seq; and single-nucleus, snRNA-seq). Initial single-cell-level studies have characterized cell types of the ocular anterior segment, including TM cells (Balasubramanian et al., 2024; Patel et al., 2020; Thomson et al., 2021; van Zyl et al., 2020; van Zyl et al., 2022), but further depth, validation, and more uniform molecular consensus/ naming of cell types are needed. This is especially true for TM cells. Currently, reports differ in the naming and definition of TM cell subtypes and offer limited validation by immunohistochemistry (IHC) or immunofluorescence (IF) on tissue sections or flat mounts.

Here we more deeply characterized the mouse TM and validated findings by immunostaining tissue sections and flat mounts and by in situ hybridization (ISH). We independently isolated and sequenced limbal cells of mice at 2 institutions and characterized the same 3 TM cell

subtypes at both. Additionally, single-nucleus assay for transposase-accessible chromatin with sequencing (snATAC-seq) identified LIM homeobox transcription factor 1 beta (LMX1B) as one of the most active transcription factors in TM cells. Variants in *LMX1B* cause IOP elevation and glaucoma (Choquet et al., 2018; Gao et al., 2018; Gharahkhani et al., 2021; Khawaja et al., 2018; MacGregor et al., 2018; Shiga et al., 2018). By analyzing *Lmx1b*$^{V265D/+}$ mutant mice (develop elevated IOP and glaucoma, Cross et al., 2014; Tolman et al., 2021), we show that mitochondrial pathways are primarily disturbed in the TM3 cell subtype, which most strongly expresses *Lmx1b*. Treatment with nicotinamide lessened IOP elevation in *Lmx1b*$^{V265D/+}$ mutants supporting testing of therapeutics that boost mitochondrial health and function in human patients.

Results

Three molecularly distinct TM cell subtypes

Using scRNA-seq, we sequenced 17,914 cells from dissected limbal tissue (contains drainage structures) of 2-month-old mice. The dataset included 13,251 cells from strain C57BL/6J (B6) and 4,663 cells from strain 129/Sj (129). The data for both strains were integrated (**Figure S1**). Computational analysis revealed six distinct clusters of cells that were TM-containing, epithelia, pigmented epithelia (iris and ciliary body), endothelial, immune and neuron (**Figure 1A**). The identity of each of these cell clusters was based on various well-characterized marker genes (**Figure S2A-B**, Balasubramanian et al., 2024; Thomson et al., 2021; van Zyl et al., 2020). There were no major differences in the distributions of strain B6 and strain 129 cells within the relevant cell-type clusters (**Figure S3A-C**). Therefore, to improve statistical power, downstream analyses used the integrated dual-strain dataset.

Cells of cluster 1 expressed various TM genes, including *Acta2* (α-SMA), *Pitx2*, *Tfap2b*, and *Myoc* (**Figure S2A-B**, Akula et al., 2020; Balasubramanian et al., 2024; de Kater et al., 1992; Ostojic et al., 2008; van Zyl et al., 2020). Unbiased sub-clustering of Cluster 1 revealed 10 distinct sub-clusters (**Figure 1B**), which included three TM cell clusters based on signature gene expression (**Figure 1D-E**). We named these clusters TM1, TM2, and TM3. Hierarchical clustering of these cell types indicated that TM1 and TM2 are more molecularly similar to each other than to TM3 (**Figure 1C**). The remaining seven clusters were identified as cells from other ocular tissue including the iris stroma, sclera, corneal keratocytes, corneal endothelium, ciliary

muscle, pericytes, and Schwann cells (**Figure S2C**, Liu et al., 2003; Lopez et al., 2009; Monje et al., 2018; Nitzan et al., 2013; Patel and Parker, 2015; Stratton et al., 2017; Toyono et al., 2015; van Zyl et al., 2022).

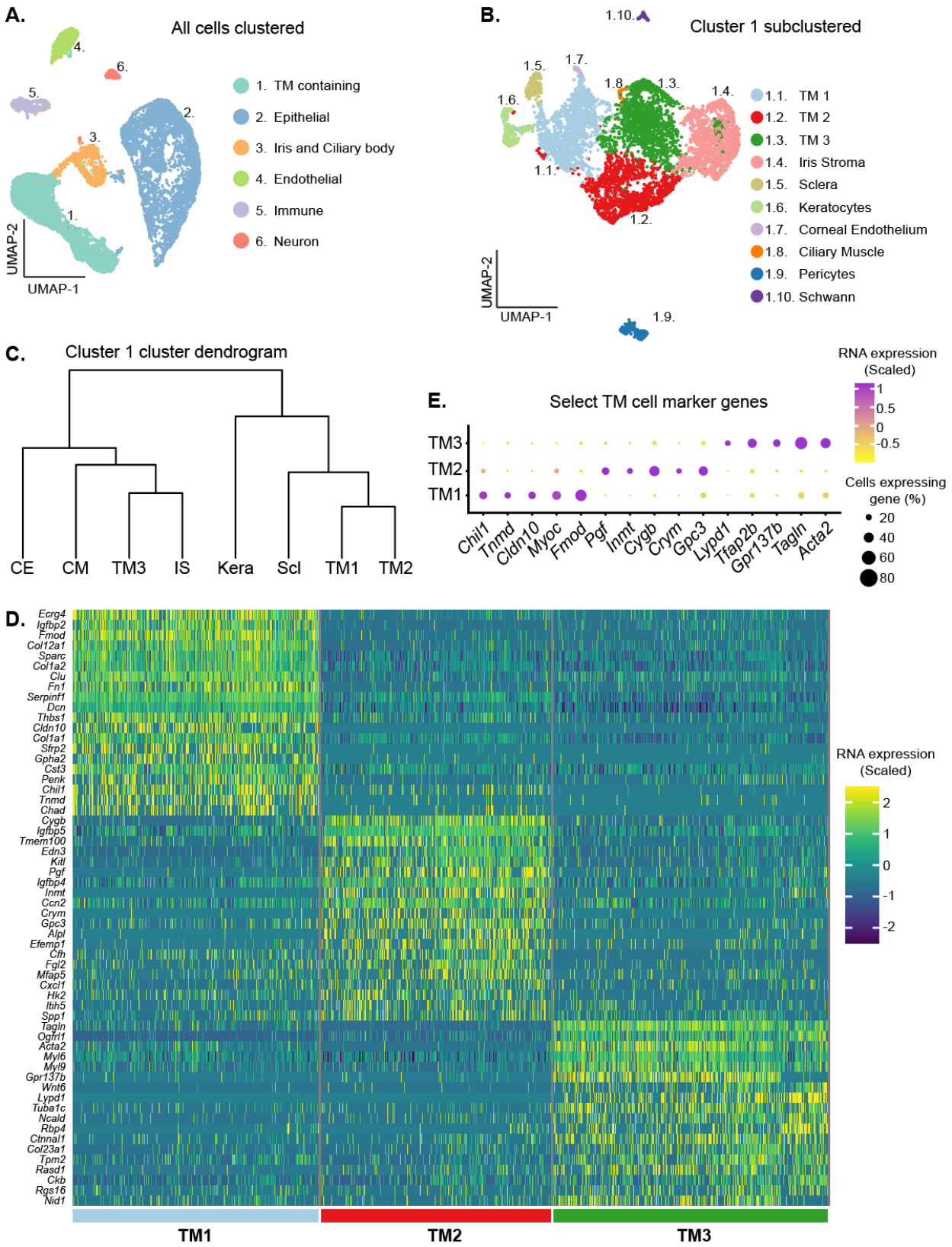

Figure 1: scRNA-seq data identifies three TM cell clusters. (A) Cells from limbal tissue dissected and sequenced at Columbia University (integrated B6 and 129/Sj datasets) are

depicted in clusters on a UMAP space. **(B)** UMAP representation of subclustered trabecular meshwork (TM) containing cluster. Three distinct TM cell clusters are identified (TM1, TM2, and TM3). **(C)** Dendrogram illustrating the relationships among these subclusters. TM1 and TM2 are more similar to each other than to TM3. **(D)** Heatmap showing the signature genes for TM1, TM2, and TM3 cells. The scaled RNA expression indicates how many standard deviations a given gene's expression is from the average expression across all examined cells (positive value is greater than the expression average and negative values are lower than expression average). **(E)** The scaled expression of select marker genes that robustly differentiate TM cell subsets from each other are shown with a dot plot. CE: corneal endothelium, CM: ciliary muscle, IS: iris stroma, Kera: corneal keratocytes, Scl: scleral.

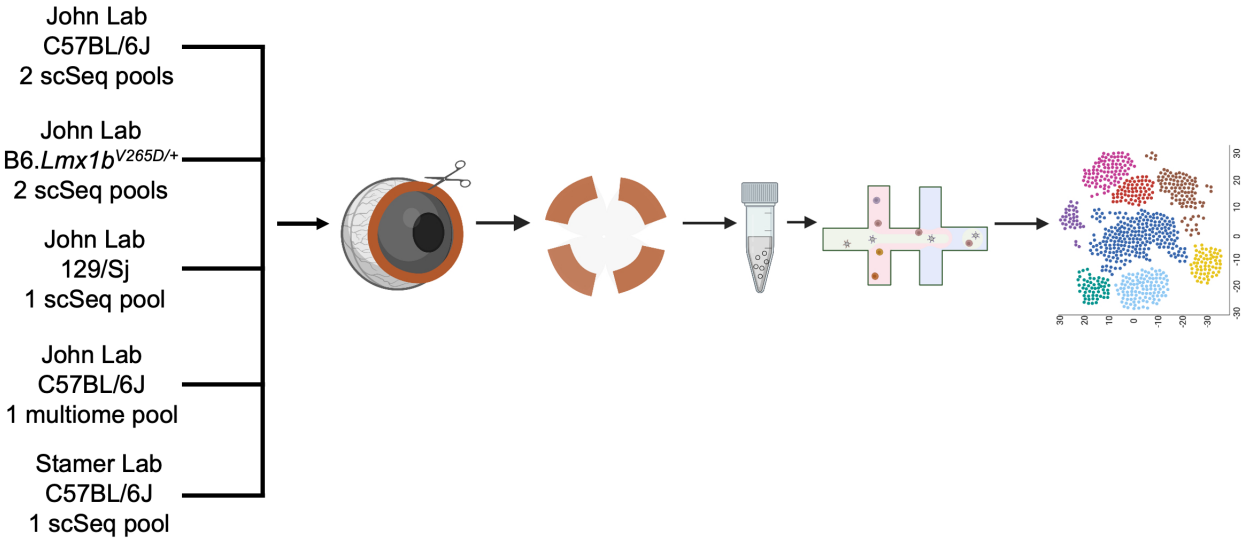

Supplemental Figure 1: Schematic of datasets and pipeline. Each pool included limbal tissue from 8 eyes. The mouse strains and lab where data was generated are shown (Columbia University, John Lab or Duke, Stamer lab). Individual eyes were dissected to isolate a strip of limbal tissue enriched for TM cells. Limbal strips were then minced and pooled for further processing. Individual cells were sequenced using the 10X Genomics pipeline (see Methods) for sc-RNA-Seq or multiome (snRNA-seq and scATAC-seq). Schematic created with BioRender.com

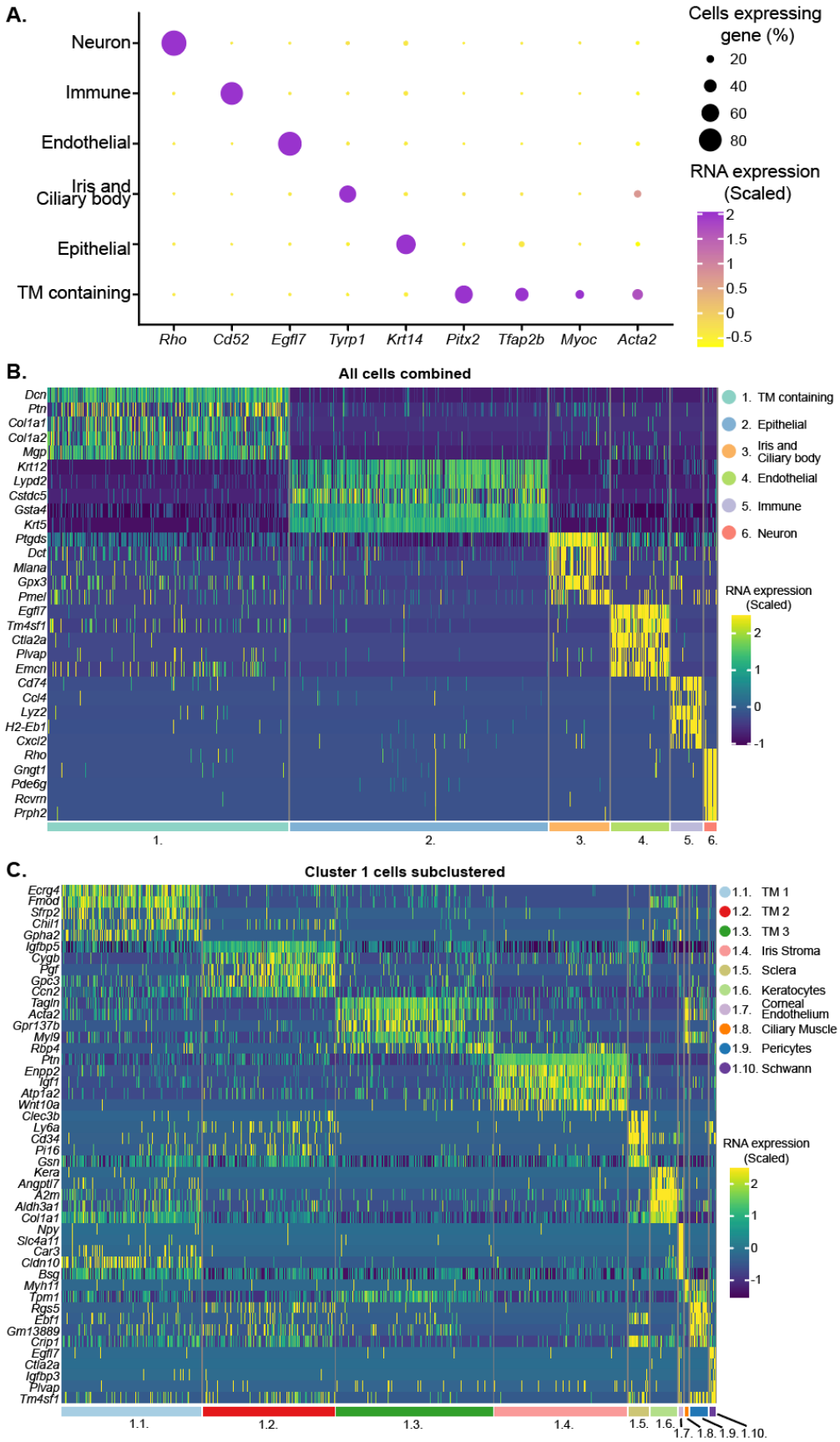
A.
Neuron
Immune
Endothelial
Iris and Ciliary body
Epithelial
TM containing
Rho
Cd52
Egfl7
Tyrp1
Krt14
Pitx2
Tfap2b
Myoc
Acta2
Cells expressing gene (%)
20
40
60
80
RNA expression (Scaled)
2
1.5
1
0.5
0
-0.5
B.
All cells combined
Dcn
Ptn
Col1a1
Col1a2
Mgp
Krt12
Lypd2
Cstdc5
Gsta4
Krt5
Ptgds
Dct
Mlana
Gpx3
Pmel
Egfl7
Tm4sf1
Ctla2a
Plvap
Emcn
Cd74
Ccl4
Lyz2
H2-Eb1
Cxcl2
Rho
Gngt1
Pde6g
Rcvrn
Prph2
1. TM containing
2. Epithelial
3. Iris and Ciliary body
4. Endothelial
5. Immune
6. Neuron
RNA expression (Scaled)
2
1
0
-1
1.
2.
3.
4.
5.
6.
C.
Cluster 1 cells subclustered
Ecrg4
Fmod
Sfrp2
Chil1
Gpha2
Igfbp5
Cygb
Pgf
Gpc3
Ccn2
Tagln
Acta2
Gpr137b
Myl9
Rbp4
Ptn
Enpp2
Igf1
Atp1a2
Wnt10a
Clec3b
Ly6a
Cd34
Pi16
Gsn
Kera
Angptl7
A2m
Aldh3a1
Col1a1
Npy
Slc4a11
Car3
Cldn10
Bsg
Myh11
Tpm1
Rgs5
Ebf1
Gm13889
Crip1
Egfl7
Ctla2a
Igfbp3
Plvap
Tm4sf1
1.1. TM 1
1.2. TM 2
1.3. TM 3
1.4. Iris Stroma
1.5. Sclera
1.6. Keratocytes
1.7. Corneal Endothelium
1.8. Ciliary Muscle
1.9. Pericytes
1.10. Schwann
RNA expression (Scaled)
2
1
0
-1
1.1.
1.2.
1.3.
1.4.
1.5.
1.6.
1.7.
1.8.
1.9.
1.10.

Supplemental Figure 2: Limbal cell cluster marker genes. (A) The expression levels of various anterior segment cell type marker genes in the integrated B6 and 129 data are depicted on a dot plot. These marker genes are generally accepted to be specific to individual cell types. Epithelial cells (*Krt14*); neurons (*Rho*); endothelial cells (*Egfl7*); ciliary body and iris cells (*Tyrp1*); and immune cells (*Cd52*). Cluster 1 expressed multiple TM marker genes including *Myoc*, *Acta2* (encodes α-SMA), *Pitx2*, and *Tfap2b*. Although some of the neurons may be limbal, it is possible that others are retinal contamination. **(B-C)** Heatmaps of differentially expressed genes across all limbal tissue cell clusters (B) and across the subclusters of cluster 1 (C).

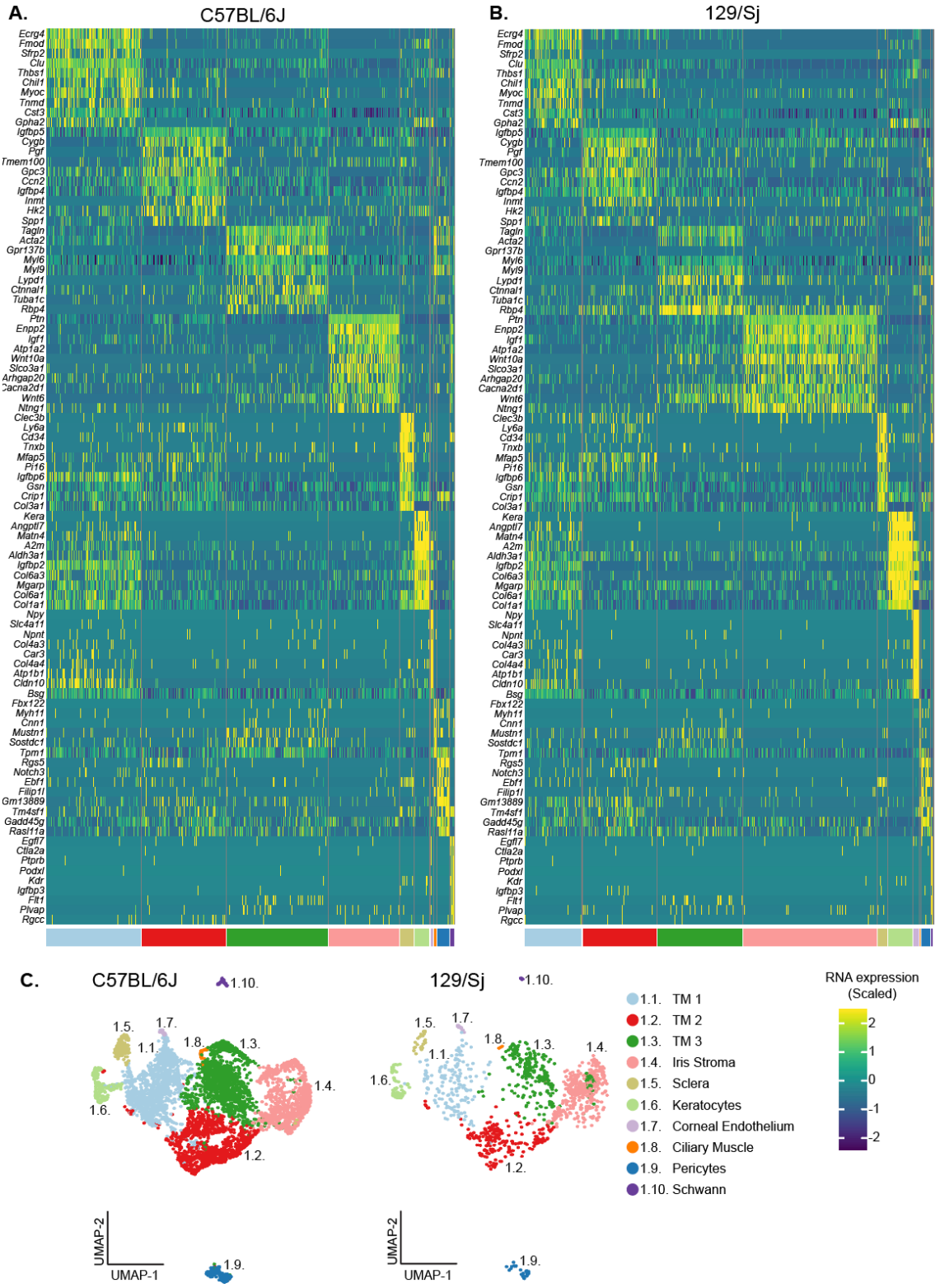

Supplemental Figure 3: Transcriptomic similarities between strain B6 and strain 129. (A-B) The 129/Sj (129) and C57BL/6J (B6) strains exhibit significant overlap in marker gene expression. Heatmaps display the expression of the top 10 gene markers for each subcluster of cluster 1. The expression patterns are very similarity across strains. **(C-D)** UMAP representations of subclusters derived from cluster 1 separated by strain.

Next, we integrated an additional limbal tissue scRNA-seq dataset (14,912 cells, Duke University) from 3 months old C57BL/6J mice with our initial 2 months old C57BL/6J dataset. Due to batch effects most likely based on differences in cell isolation techniques and environment (Columbia University vs. Duke University, see Methods), TM cells from these datasets occupied adjacent, partially overlapping, but not identical UMAP space (**Figure S4A**). Individual analysis of the Duke dataset also identified 3 TM cell subtypes with the same marker gene expression and enriched molecular pathways compared to the Columbia University data (**Figure S4B-E**, **Table S1**). In datasets from previous mouse limbal scRNA-seq studies, there was also a high degree of overlap of marker gene expression with our 3 TM cell clusters (**Figure S5A-B**, **Table S2**, Thomson et al., 2021; Ujiie et al., 2023; van Zyl et al., 2020). However, some TM subtype clusters reported in previous studies expressed genes that overlapped with both of our TM2 and scleral cell clusters. (**Figure S5B-C**, Thomson et al., 2021; van Zyl et al., 2020). To resolve this discrepancy, we performed IF for two of the discordantly annotated markers previously reported to be expressed in TM cells but present in our scleral cluster (CD34 and LY6C1). This immunolabeling showed that these markers are expressed in scleral but not TM cells (**Figure S6A-B**). In addition, in previous studies, cells with markers matching TM3 (e.g. *Lypd1*) were named uveal cells without IF confirmation (Thomson et al., 2021; Ujiie et al., 2023; van Zyl et al., 2020). IF revealed that our TM3 cells are neither located in the uvea nor abundant in the uveal adjacent TM but primarily reside in the anterior TM closer to the cornea (see below).

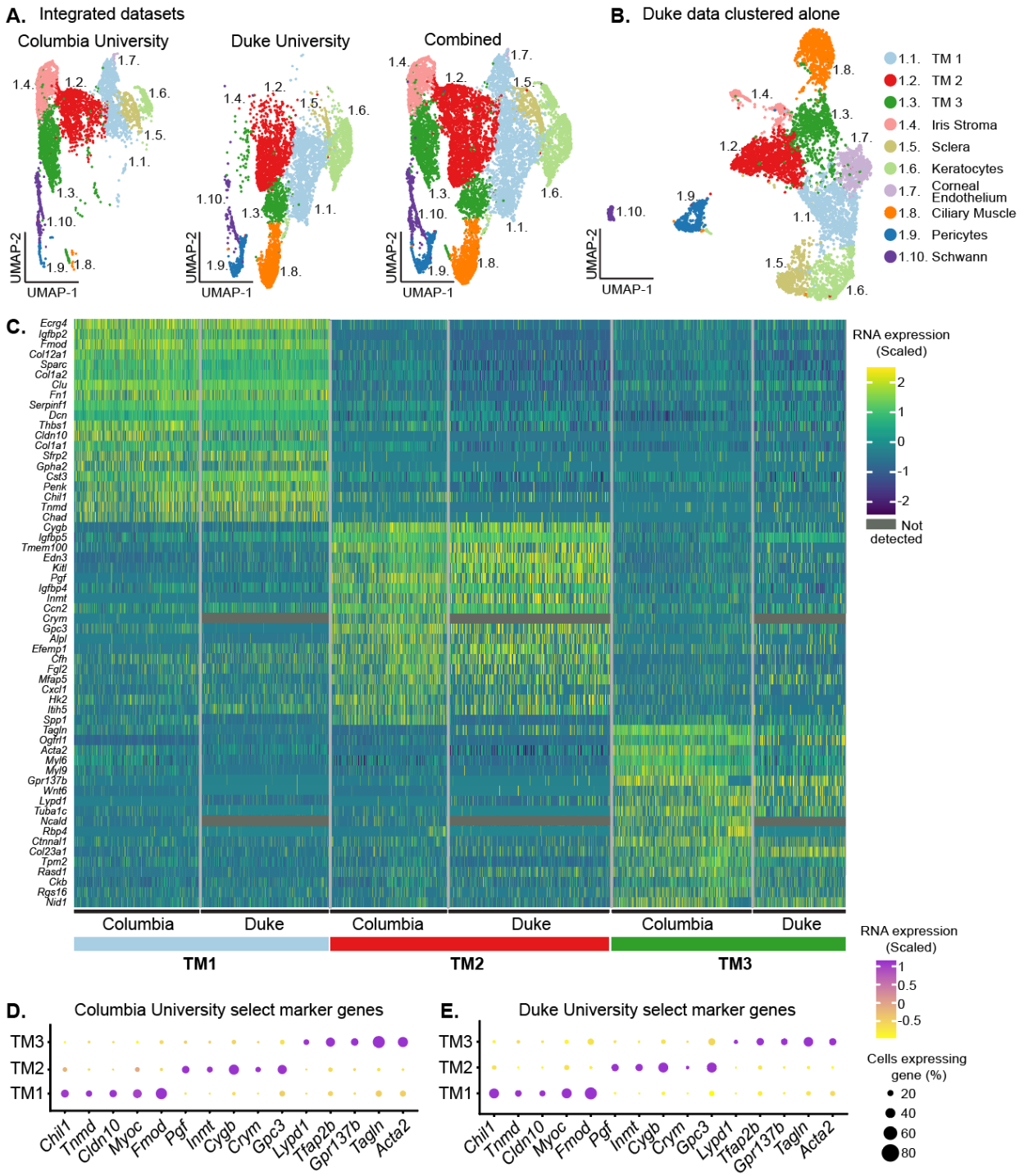

Supplemental Figure 4: An independent B6 scRNA-seq dataset corroborates TM cell clusters. (A) UMAPs of the integrated Columbia University and Duke University datasets. Cells from the different institutions occupy largely different but adjacent UMAP coordinates with some overlap, indicating batch effects. The difference was largest for TM3, but the marker genes were still conserved. This was likely driven by differences in tissue processing methods (Duke dataset, Methods). **(B)** Analysis of Duke University data alone independently validates our findings presented in *Figure 1* from Columbia University, including the presence of 3 TM cell clusters. **(C)**. A heatmap comparing the top 20 marker genes of each TM cell subcluster for the

Columbia (C57BL/6J strain only) and Duke datasets. Overall, there is strong overlap of TM cell gene expression between datasets. Discrepancies include certain marker genes (eg. *Crym*) in the Columbia dataset that are not detected in the Duke dataset. These differences are associated with lower sequencing depth in the Duke data, and other technical factors/batch effects. **(D-E)** Dot plots showing similar TM subtype marker gene expression in the two datasets.

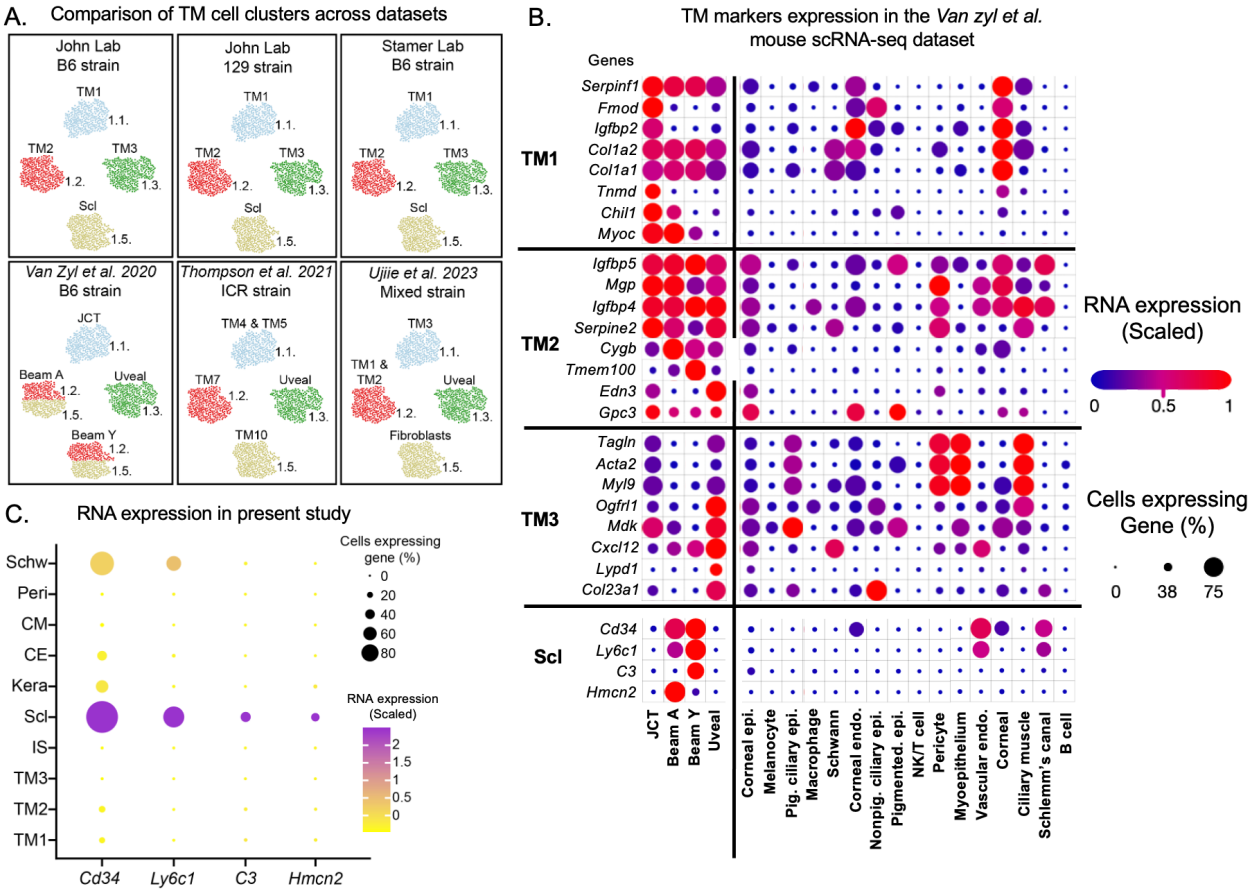

Supplemental Figure 5: Comparison of our TM cells to published mouse datasets (A) Diagrammatic representation of TM and scleral cell clusters across different mouse scRNA-seq datasets. **Upper panels** diagrammatically represent the current study. **Lower panels** represent the indicated studies. All diagrams based on marker gene expression in the cells that were clustered together. Despite some naming differences, matches for the 3 TM cell types that we identify in the current paper are evident in the previous studies. Although previous studies named additional TM subtypes, we did not subcluster to the same degree to ensure that subtype differences are robust. Previous studies had limited if any validation for some cell types. Based on our current characterization and immunofluorescent localization studies (Figures 2, S6, S8, & S9) some of the cells previously labeled TM beam cells are scleral (possibly fibroblasts). The marker gene expression for these previously named TM beam cells is highest in 'Fibroblasts' rather than TM cells in human scRNA-seq data, further supporting a scleral identity. In addition, cells previously named as uveal cells are a TM cell type. The cells are color-coded based on their molecular identities to match the current study. Current study subcluster identity numbers are shown. **(B)** Dot plot of TM cell subtype markers identified in the present study (left) using the dataset and cell type assignments (bottom) of Van Zyl et al. Based on these markers, our TM subtypes match their data as follows: TM1= JCT, TM2 = Beam A and Beam Y, and TM3 = Uveal). Scleral markers that we found are enriched in the Van Zyl Beam A and Y cells, which appear to be a mix of different cell types. **(C)** Expression of the Van Zyl Beam A and Y cell markers that are enriched in sclera in our combined B6 and 129 dataset (the same expression pattern was evident in all Columbia and Duke datasets in the current study). See Figure S6 for IF showing expression of these markers in Sclera but not TM.

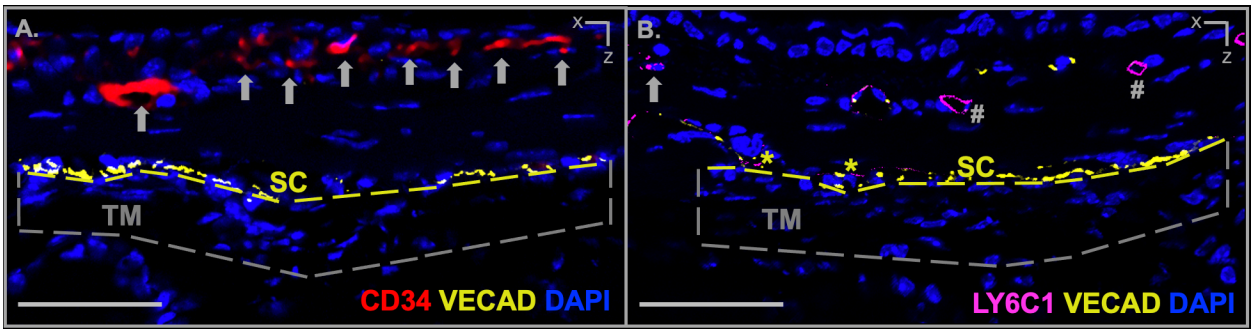

Supplemental Figure 6: Immunostaining demonstrates expression of specific marker genes in sclera but not TM (see Figure S5). (**A**) CD34 is expressed in cells of the sclera/corneoscleral transition zone (arrows). No CD34 staining was found in the TM (> 60 sections from 4 eyes). **(B)** LY6C1 is expressed in the sclera. In addition to nonvascular cells (arrow), LY6C1 was expressed in vascular cells within the sclera (based on morphology and the vascular endothelial cell marker, VECAD, hash marks) and SC (yellow asterisks). LY6C1 is not found in the TM. The TM is encompassed within the dashed box while the yellow dashed line marks the inner wall of SC (see Figure S7). Scale bars = 50 μm.

TM subtypes differentially occupy TM zones

To further explore the sub-anatomical localization of the TM cell subtypes, we used a combination of IF and ISH to identify subtype markers. Each TM cell subtype had a higher percentage of cells expressing, and an increased average expression of, its respective subtype markers (all P < 1E-100) compared to other TM cells, **Figure S7A**). To analyze the distribution of subtypes, we first divided the TM into zones along its anterior/posterior and inner/outer axes (**Figure S7B-E**). The total area of TM occupied by each individual subtype marker was assessed in each zone on more than 150 tissue sections. This detected biases for the subtypes to be differentially localized in specific TM zones (**Figure 2A-F**). For instance, TM1 cells were significantly more frequent in the posterior and outer TM zones, while TM3 cells were overrepresented in the anterior and inner zones (all P < 0.01). The different marker molecules that were assessed for each TM cell subtype gave highly consistent results regarding zonal occupancy (**Figure S8A-B, Figure S9**). In addition, we confirmed the localization biases in 3D whole mounts of the mouse limbus (Kizhatil et al., 2014, for TM1: MYOC and TM3: α-SMA markers; **Figure 2G-H**). Collectively, these data indicate clear localization biases that differ for the TM1 and TM3 subtypes.

To better understand the location of TM cell subtypes, we analyzed marker expression patterns in 50-60 exceptionally high-quality sections for each marker of each TM cell subtype (see

Methods). For this analysis, the TM was divided into eight regions (**Figure S7F**). Not only did this refine the localization bias of TM1 and TM3 cells, but it discovered that TM2 cells are most concentrated in the mid-posterior two-thirds of the TM (mid regarding inner-outer axis, all $P < 0.01$, **Figure 2I-K**). Despite their biased distributions, some cells of each TM subtype were detected in most TM regions.

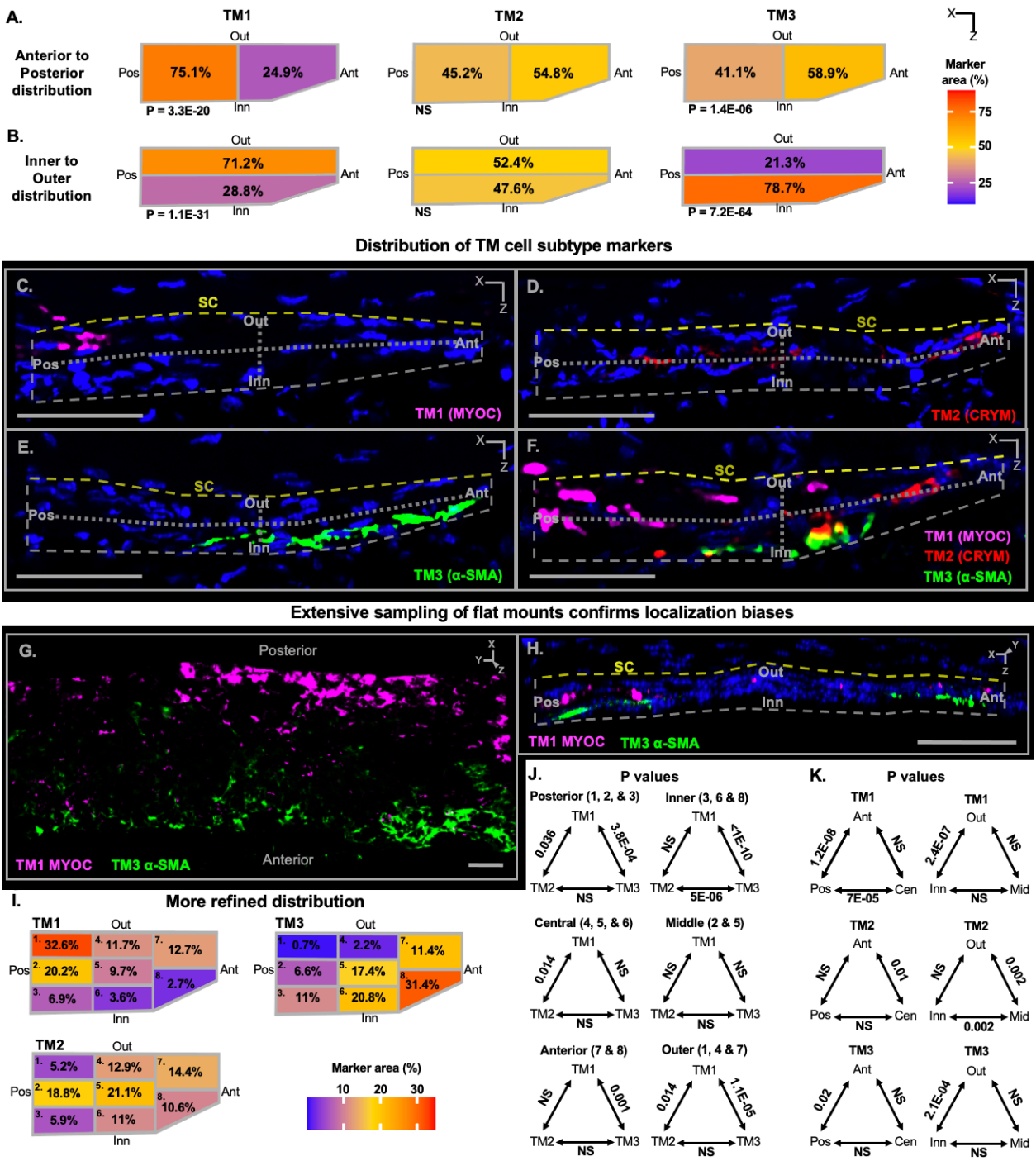

Figure 2: Biased localization of TM cell subtypes within the TM. (A-B) Summary diagrams showing the location of expression of TM1, TM2, and TM3 signature markers in the TM. For quantification of marker distributions, the TM was divided in half along both anterior-posterior (A) and inner-outer (B) axes (see Figure S7 localization of TM and SC). The area of the TM that was positive for each marker within each region was calculated as a percentage of the total area occupied by that marker in the entire TM on each section. The percentage of marker localization to each region was averaged across all analyzed sections. The average localization across all markers used for each TM cell subtype (see Figure S8 and S9) is shown on the diagrammatic representations of the TM using heatmaps. TM1 localization is biased towards the

posterior and outer TM, whereas TM3 is biased towards the anterior and inner TM. No clear bias for TM2 was observed. A total of 286 sections were examined using immunofluorescence (IF) and in situ hybridization (ISH). Between 130-160 sections were examined for each TM cell subtype. **(C-F)** Representative sections for a subset of markers for each subtype used for quantification. See Figure S6 for explanation of indicated tissue orientations. **(G)** En face image of the TM in a 3D reconstruction of a tissue whole mount, clearly demonstrating the anterior vs posterior localization bias for TM1 (posterior bias) and TM3 (anterior bias) cell types. **(H)** Orthogonal 3D image that is cropped and oriented in the same planes as the tissue sections. The inner bias for α-SMA (*Acta2*, TM3) compared to an outer bias for MYOC (TM1) is evident. **(I)** More spatially refined analyses were subsequently conducted using extremely high-quality sections (50-60 per marker) by dividing the TM into 8 smaller zones (see Figure S7. In this more refined study, TM2 cells have a biased localization to a posterior and central region of TM (most enriched in zones 2 and 5, see Figure S7. **(J-K)** The TM subtype distributions were statistically compared across the combined zones (in parentheses) as indicated. ANOVA followed by Tukey's honestly significant difference test. Ant: anterior TM, Pos: posterior TM, Inn: inner TM, Out: outer TM, SC: Schlemm's canal. Grey dotted lines mark the TM zones, yellow dotted lines mark inner wall of Schlemm's canal. All scale bars: 50 μm.

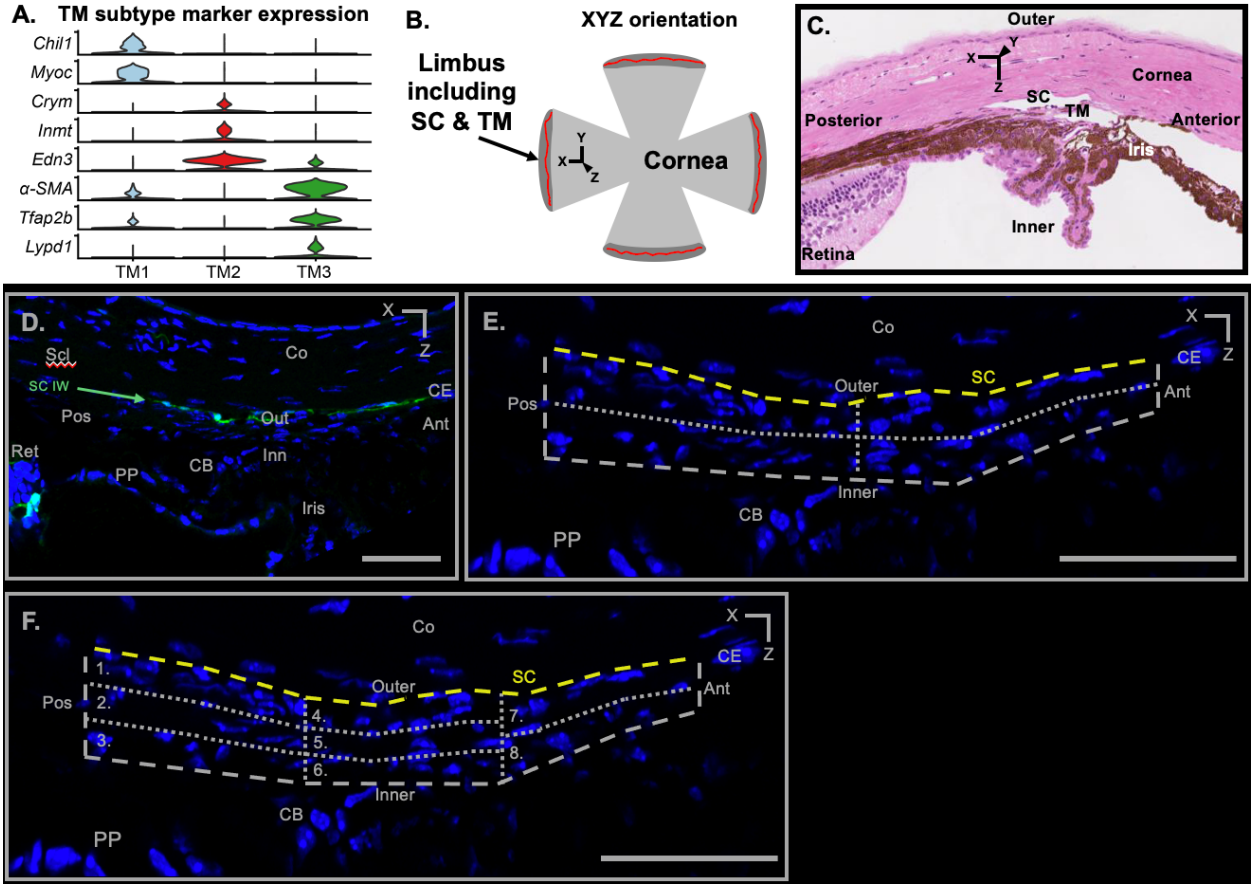

Supplemental Figure 7: Assessing zonal distribution of TM cell subtypes. (A) Violin plot showing expression of signature genes that were used to localize TM cell subtypes. **(B-C)** Diagram of flat-mounted anterior segment (B) and *hematoxylin and eosin*-stained *s*agittal section (C) indicating the X, Y and Z axis as used throughout this paper as previously reported (Kizhatil et al., 2014)**. (D-E)** Schlemm's canal (SC) inner wall was identified based on anatomy and the expression of *Prox*-GFP (green) and other endothelial cell markers. The pars plana (PP) and corneal endothelium (CE) were identified based on anatomy and DAPI staining. The posterior boundary of the TM begins just anterior to the PP and was typically aligned with the most posterior portion of SC. The anterior TM ends where the corneal endothelium begins. This typically aligned with the most anterior portion of SC. The outer boundary of the TM was immediately internal to the inner wall of SC. The inner-most TM was where the TM cells end abutting the anterior chamber. Using these boundaries, the anterior-posterior and inner-outer axis of the TM were measured. Based on these measurements for each eye, the TM was divided in half along both the inner-outer and anterior-posterior axes. (**F**) For more refined analysis, the anterior-posterior distance was then divided into thirds to generate posterior, central, and anterior regions. Each of these regions was then equally divided into their subregions as shown. Because the anterior TM is thinner, it was divided into two zones. These divisions generate 8 TM zones. All scale bars: 50 μm.

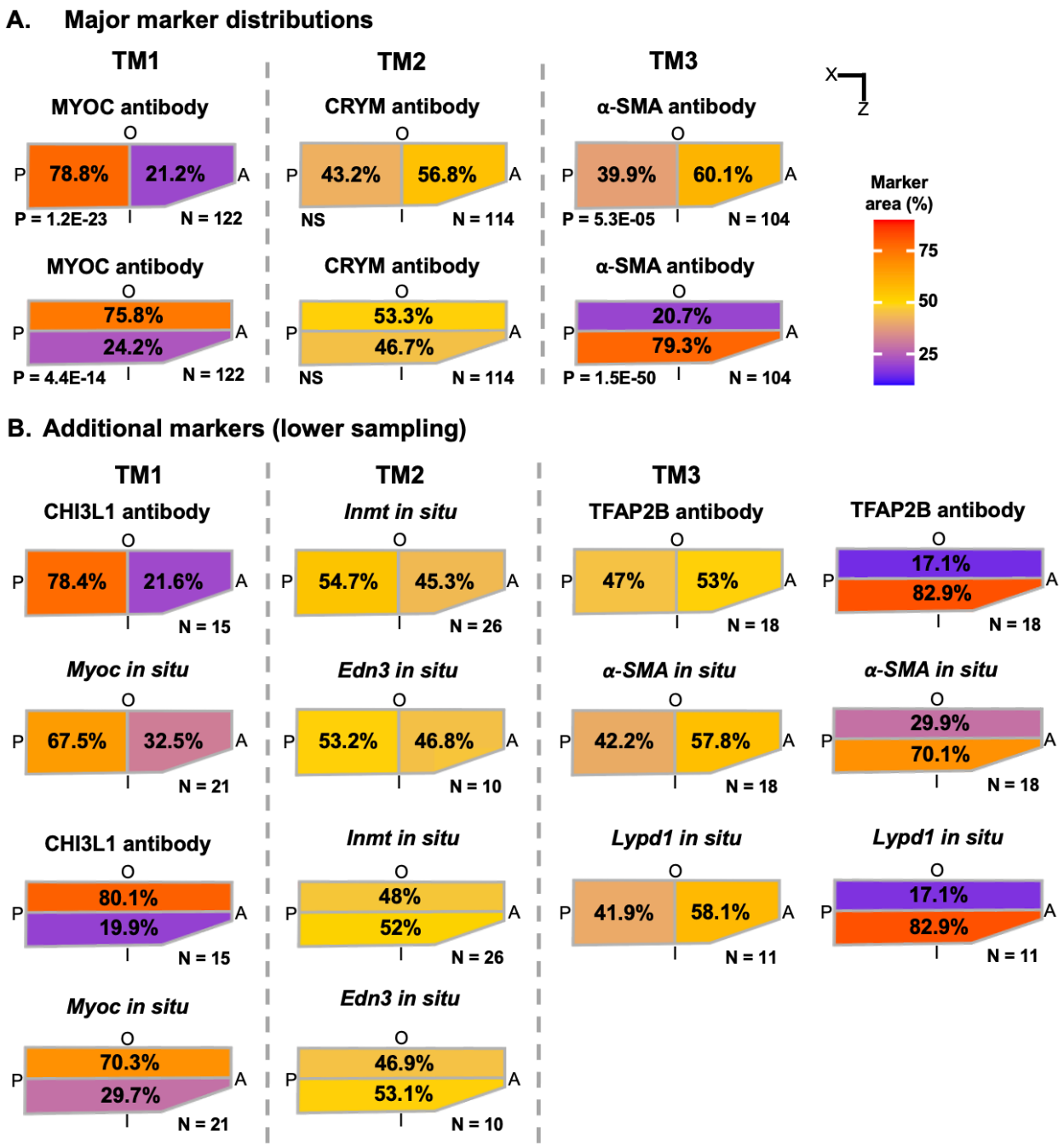

Supplemental Figure 8: Distribution of TM cell subtypes by marker. (A) Schematic representation of major marker distributions from Figure 2. **(B)** Additional markers for a given TM cell subtype had similar patterns of localization (see Figure S9 for example staining). However, these markers were not sampled deeply enough to perform statistical analysis. A: anterior TM, I: inner TM, O: outer TM, P: posterior TM.

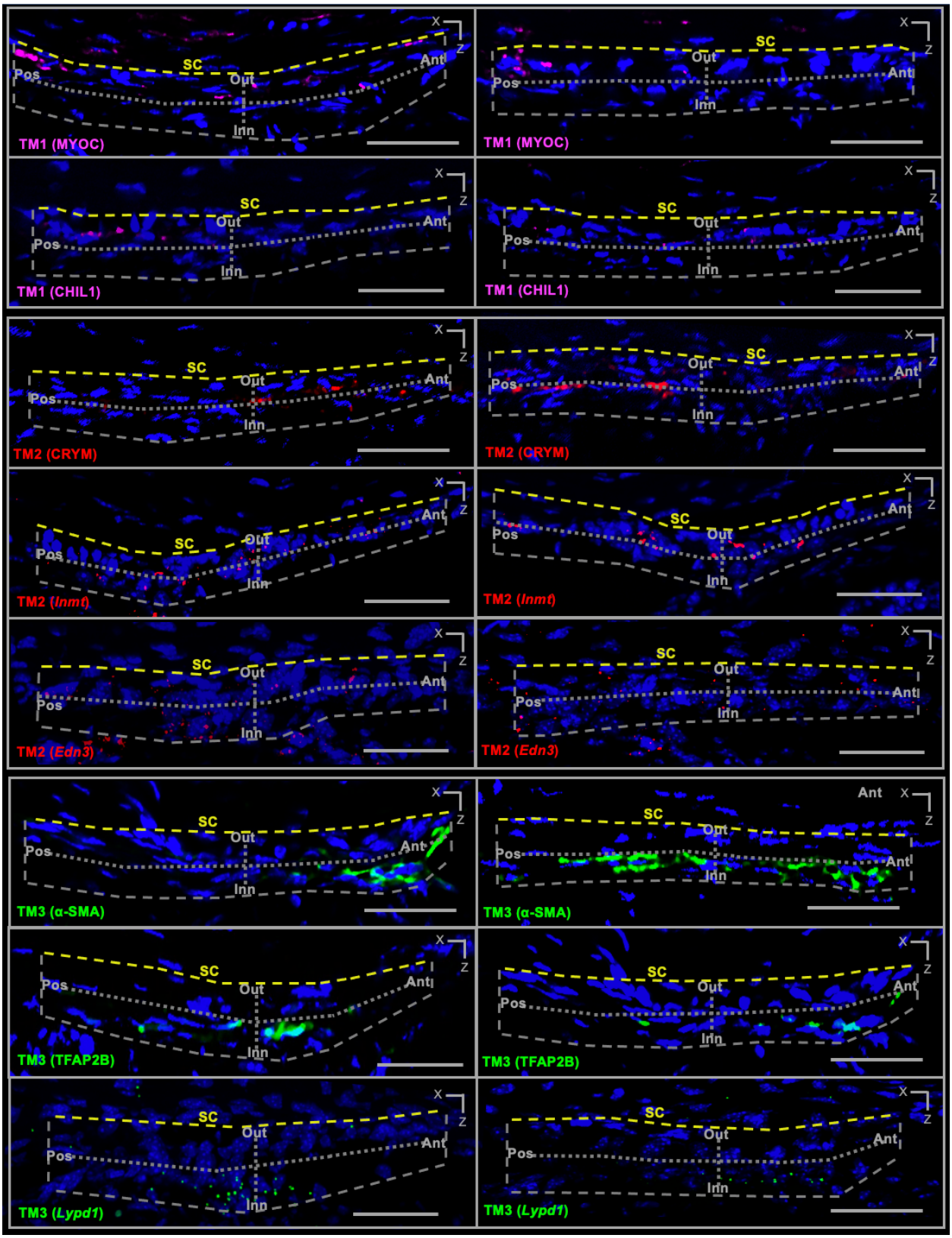

Supplemental Figure 9. Additional examples of TM subtype marker localization. Although there is variability in expression between sections, the aggregate of all sections reveals the biased distributions of TM cell subtypes as summarized in Figures 2. Here we focus on TM

expression. However, some of the markers are also expressed outside of the TM. For examples, *Edn3* is expressed in vasculature, while both *Lypd1* and *Inmt* are expressed at low levels in scleral and iris cells (but are significantly higher in TM cells). All scale bars: 50 μm. Markers assessed by IF: MYOC, CHIL1, CRYM, α-SMA, TFAP2B. Markers assessed by ISH: *Inmt*, *Edn3*, *Lypd1*. All scale bars: 50 μm.

Molecular comparison of TM cell subtypes

To determine the molecular functions of TM cells, we first conducted gene ontology (GO) analysis using genes that were differentially expressed genes (DEGs) in all TM cells as a group compared to other sequenced cells (**Table S3**). Additionally, we used gene set enrichment analysis (GSEA) to assess whether these GO pathways are relatively enriched or underrepresented in TM cells. Compared to other cells, TM cells were enriched for pathways associated with extracellular matrix (ECM) structure and function, including signaling associated with collagens, proteases, integrins, and glycosaminoglycans (**Figure 3A**, **Figure S10A**, **Table S4**). TM cells were also enriched for growth factor signaling. Conversely, underrepresented pathways in TM cells were associated with desmosomes, peroxisomes, and certain cytoskeletal and plasma membrane elements. These pathways help define TM cells relative to other cells in the region.

Next, we compared TM cell subtypes to each other (**Figure 3B-D**). TM1 cells were most enriched for ECM pathways, particularly structural components such as collagens, integrins, and other ECM elements (**Figure 3B**, **Figure S10B**). The expression of several ECM genes that are reported to impact IOP are heightened in TM1 cells, including Type VIII collagens, fibronectin, and *Ltbp2* (Ali et al., 2009; Desronvil et al., 2010; Roberts et al., 2020). Both TM1 and TM2 cells have enriched expression of glycosaminoglycan (GAG) genes (**Figure 3B-C**, **Figure S10B-C**). GAGs in the JCT and intertrabecular spaces form a gel-like consistency and changes in GAG abundance correlate with altered AH outflow resistance (Knepper et al., 1981; Knepper et al., 1996; Knepper and McLone, 1985). TM2 cells are uniquely enriched for the laminin complex, a key component of basement membranes (Aumailley, 2013). Pathways related to clearing debris and monitoring the extracellular environment including phagocytic vesicles, antigen presentation, and lysosomal function are also enhanced in TM2 cells. In contrast, TM3 cells are underrepresented for ECM-related pathways compared to other TM cells but are enriched for pathways related to actin binding and mitochondrial metabolism (**Figure**

3D, **Figure S10D**). The actomyosin system plays a crucial role in maintaining TM cell contractility and in regulating outflow facility (Rao et al., 2005; Syriani et al., 2009; Thieme et al., 2000; Tian and Kaufman, 2005; Zhang and Rao, 2005). The enrichment of mitochondrial metabolism pathways in TM3 cells emphasizes their energetic needs and their expected heightened susceptibility to genetic and environmental contexts that compromise metabolic functions. Importantly, genetic variation in mitochondrial/ metabolic pathways contributes risk for IOP elevation and glaucoma (Aboobakar et al., 2023; Khawaja et al., 2016; Zhang et al., 2023).

We next compared growth factor signaling and ligand-target interactions between TM cells subtypes and other cells. TM1 cells were enriched for transforming growth factor beta (TGF-β) pathway signaling (**Figure 3B**). Receptor ligand activity was enriched in TM2 cells while the membrane raft pathway (a site of signal transduction) was enriched in TM3 cells (**Figure 3C-D**). Next, we used LRLoop (Xin et al., 2022), which was developed based on NicheNet (Browaeys et al., 2020), to predict significant ligand-target interactions between TM cells and other local endothelial cells that are relevant to AH drainage (**Figure 4A-D**). TGF-β ligands (*Tgfb1*, *2*, & *3*) were predominantly expressed in TM1 cells. By contrast, TM2 cells expressed molecules critical for vascular function, such as *Angpt1*, *Vegfa*, and *Edn3* (**Figure S11A-D,** Genovesi et al., 2022; Saharinen et al., 2017; Shibuya, 2011). These TM-secreted molecules have been directly associated with SC maintenance and IOP (Comes and Borras, 2009; Fujimoto et al., 2016; Reina-Torres et al., 2017; Thomson et al., 2020).

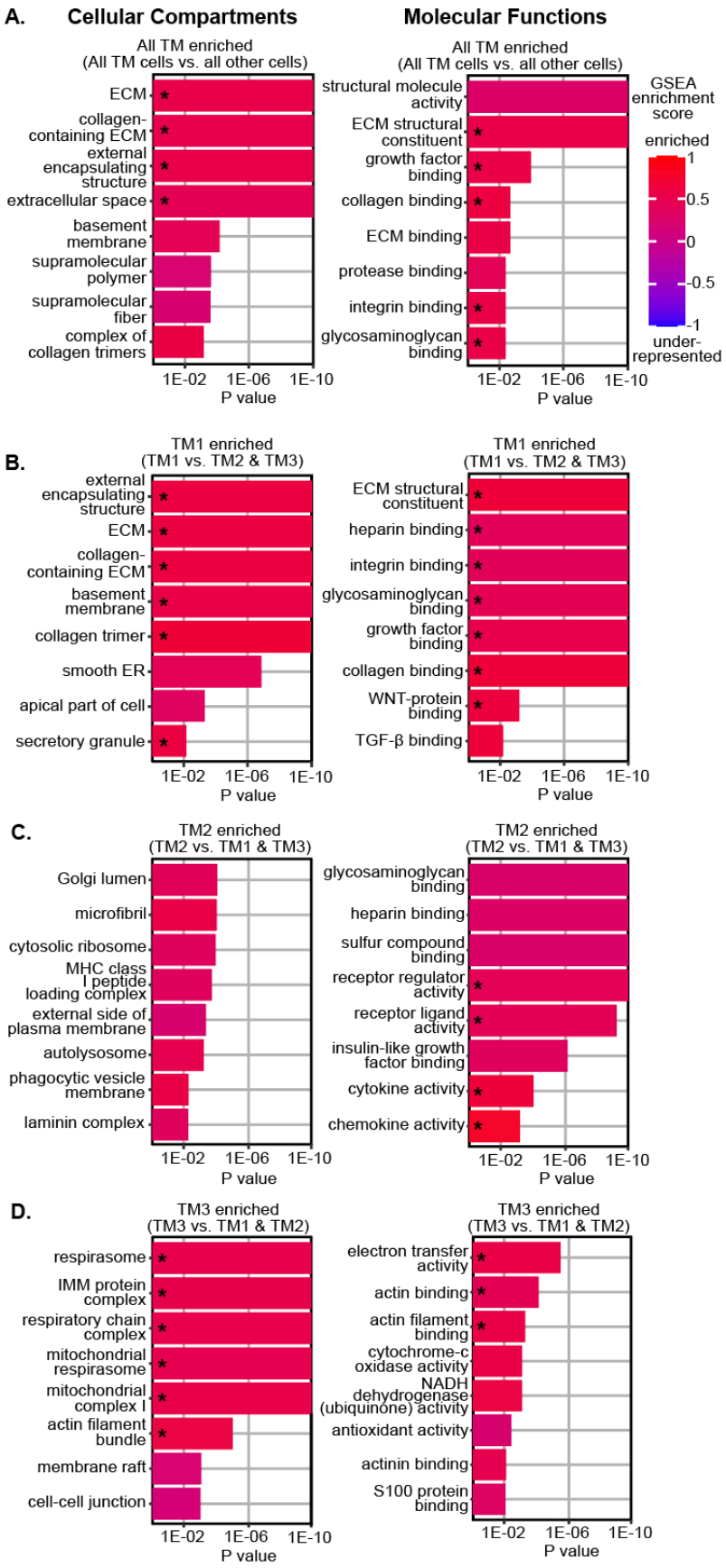
A.
Cellular Compartments
Molecular Functions
All TM enriched
(All TM cells vs. all other cells)
ECM
collagen-containing ECM
external encapsulating structure
extracellular space
basement membrane
supramolecular polymer
supramolecular fiber
complex of collagen trimers
structural molecule activity
ECM structural constituent
growth factor binding
collagen binding
ECM binding
protease binding
integrin binding
glycosaminoglycan binding
GSEA enrichment score
enriched
1
0.5
0
-0.5
-1
under-represented
1E-02
1E-06
1E-10
P value
B.
TM1 enriched
(TM1 vs. TM2 & TM3)
external encapsulating structure
ECM
collagen-containing ECM
basement membrane
collagen trimer
smooth ER
apical part of cell
secretory granule
ECM structural constituent
heparin binding
integrin binding
glycosaminoglycan binding
growth factor binding
collagen binding
WNT-protein binding
TGF-β binding
C.
TM2 enriched
(TM2 vs. TM1 & TM3)
Golgi lumen
microfibril
cytosolic ribosome
MHC class I peptide loading complex
external side of plasma membrane
autolysosome
phagocytic vesicle membrane
laminin complex
glycosaminoglycan binding
heparin binding
sulfur compound binding
receptor regulator activity
receptor ligand activity
insulin-like growth factor binding
cytokine activity
chemokine activity
D.
TM3 enriched
(TM3 vs. TM1 & TM2)
respirasome
IMM protein complex
respiratory chain complex
mitochondrial respirasome
mitochondrial complex I
actin filament bundle
membrane raft
cell-cell junction
electron transfer activity
actin binding
actin filament binding
cytochrome-c oxidase activity
NADH dehydrogenase (ubiquinone) activity
antioxidant activity
actinin binding
S100 protein binding

Figure 3: Pathway analysis suggests differential involvement of TM cell subtypes in extracellular matrix regulation, growth factor signaling, and actin-binding
(A-B) Molecular comparison of all three TM cell subtypes to all other sequenced cells using gene ontology (GO) of differentially expressed genes (DEGs). The top five most significant pathways as well as three additional pathways of interest are shown for each indicated comparison (adjusted P values, X-axis was cutoff at P < 1E-10). GSEA analysis was also used to assess the enrichment or underrepresentation of these GO pathways with GSEA scores color coded on the GO charts above. Pathways significantly different by GSEA analysis are indicated by asterisks. Overall, TM cells have over-representation of various extracellular matrix (ECM) molecules/ pathways including collagens, glycosaminoglycans, and integrins compared to non-TM cells. Growth factor signaling is also enriched in TM cells compared to other cell types. **(C-D)** When comparing TM cell subtypes, TM1 cells are further enriched for ECM molecules such as collagens, glycosaminoglycans, and integrins as well as TGF-β signaling. (**E-F**) TM2-enriched ECM pathways include glycosaminoglycan binding and the laminin complex. TM2 cells are also enriched for receptor-ligand signaling and insulin growth factor binding. **(G-H)** Actin-binding and mitochondrial metabolism genes are enriched in TM3 cells. ECM = extracellular matrix. ECS = extracellular structure. ER = endoplasmic reticulum. IMM = inner mitochondrial membrane

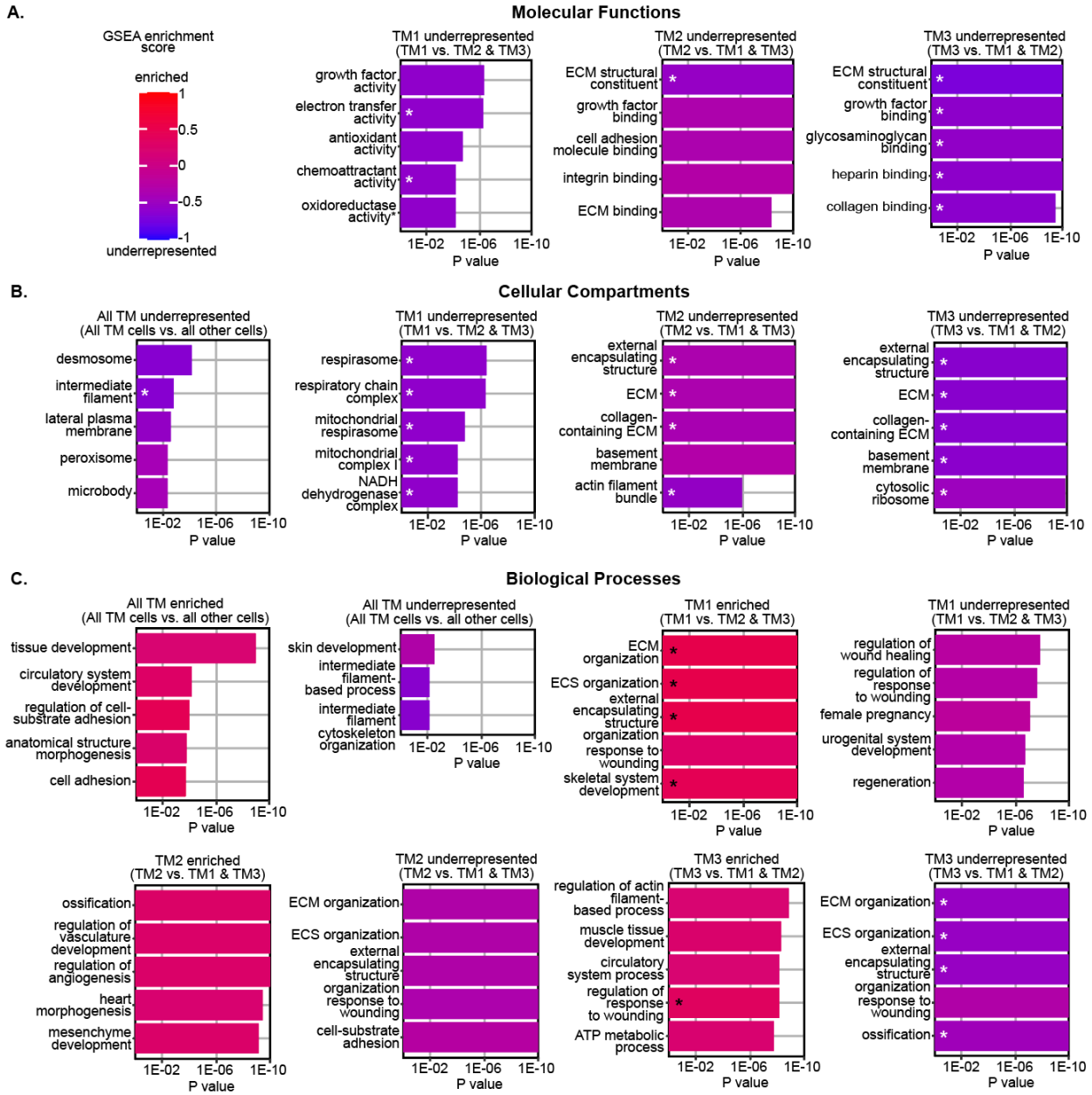

Supplemental Figure 10: TM cell pathway analysis. (A-C) Additional analyses showing the most significant pathways (by gene ontology (GO) analysis. Pathways are further separated into enriched or underrepresented categories based on gene set enrichment analysis (GSEA) score. Asterisks indicate pathways that are significantly enriched or underrepresented based on GSEA score. ECM = extracellular matrix. ECS = extracellular structure.

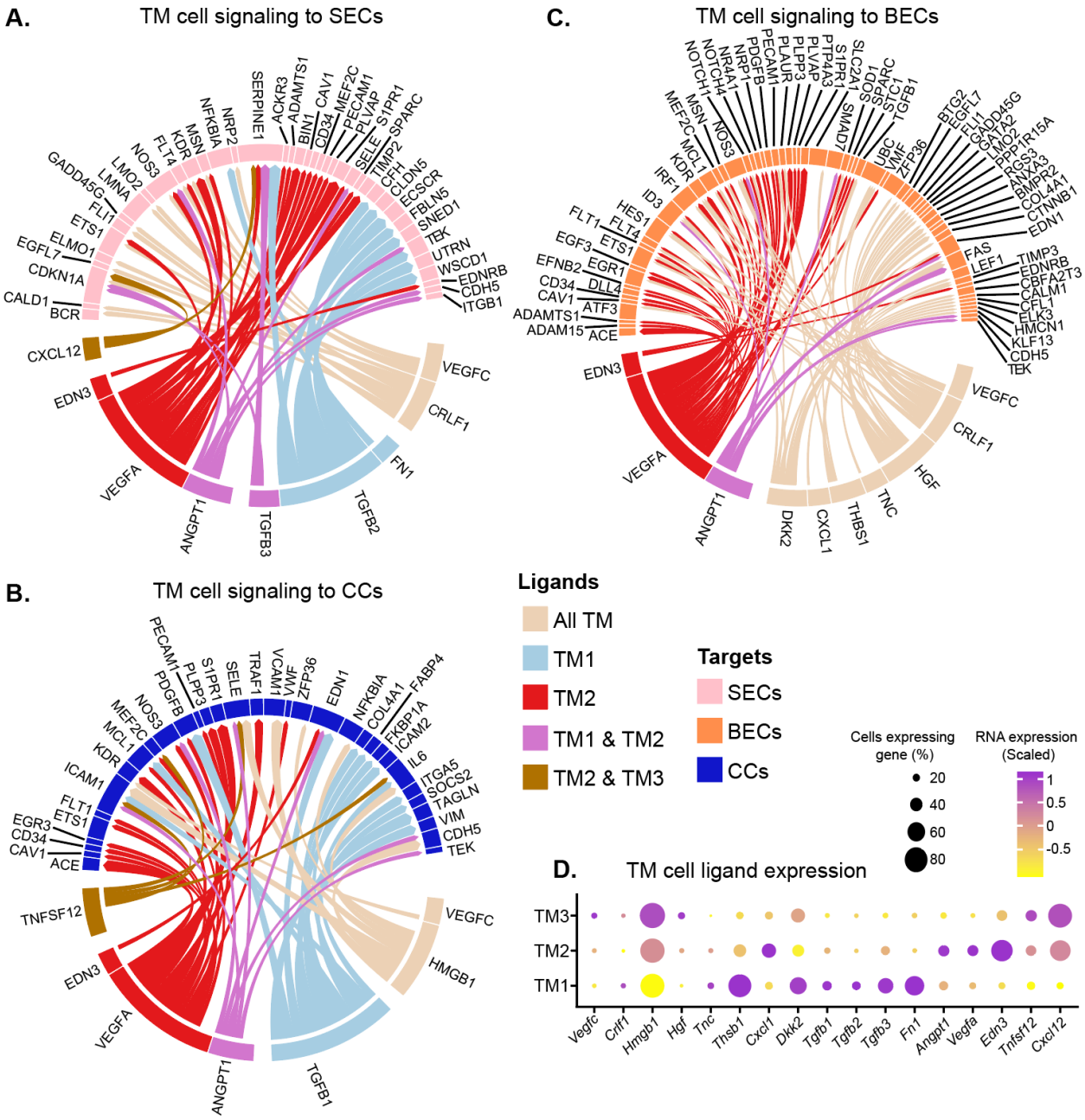

Figure 4: Signaling interactions directed from TM cells to Schlemm's canal and vascular endothelial cells differ across TM subtypes. (A) Circos plot showing the top predicted interactions between TM cell ligands and Schlemm's canal endothelial (SEC) target molecules. The top predicted targets in all TM cells are split by their expression across subtypes. TM1 and TM2 participate in more predicted signaling events compared to TM3. TM1-biased ligands include members of the *Tgf-β* and fibronectin signaling families. Various endothelial trophic factors are predominantly expressed in TM2 including endothelin 3, vascular endothelial growth factor A, and angiopoietin 1. See Table S5 for comprehensive list of ligand-target interaction data. **(B-C)** TM cell ligands that signal to collector channel (CC) endothelial cells (B) or blood endothelial cells (BECs, C). **(D)** The expression of all ligands predicted to have signaling interactions with SECs, CCs, or BECs, are displayed across TM cell subtypes (Dot plot).

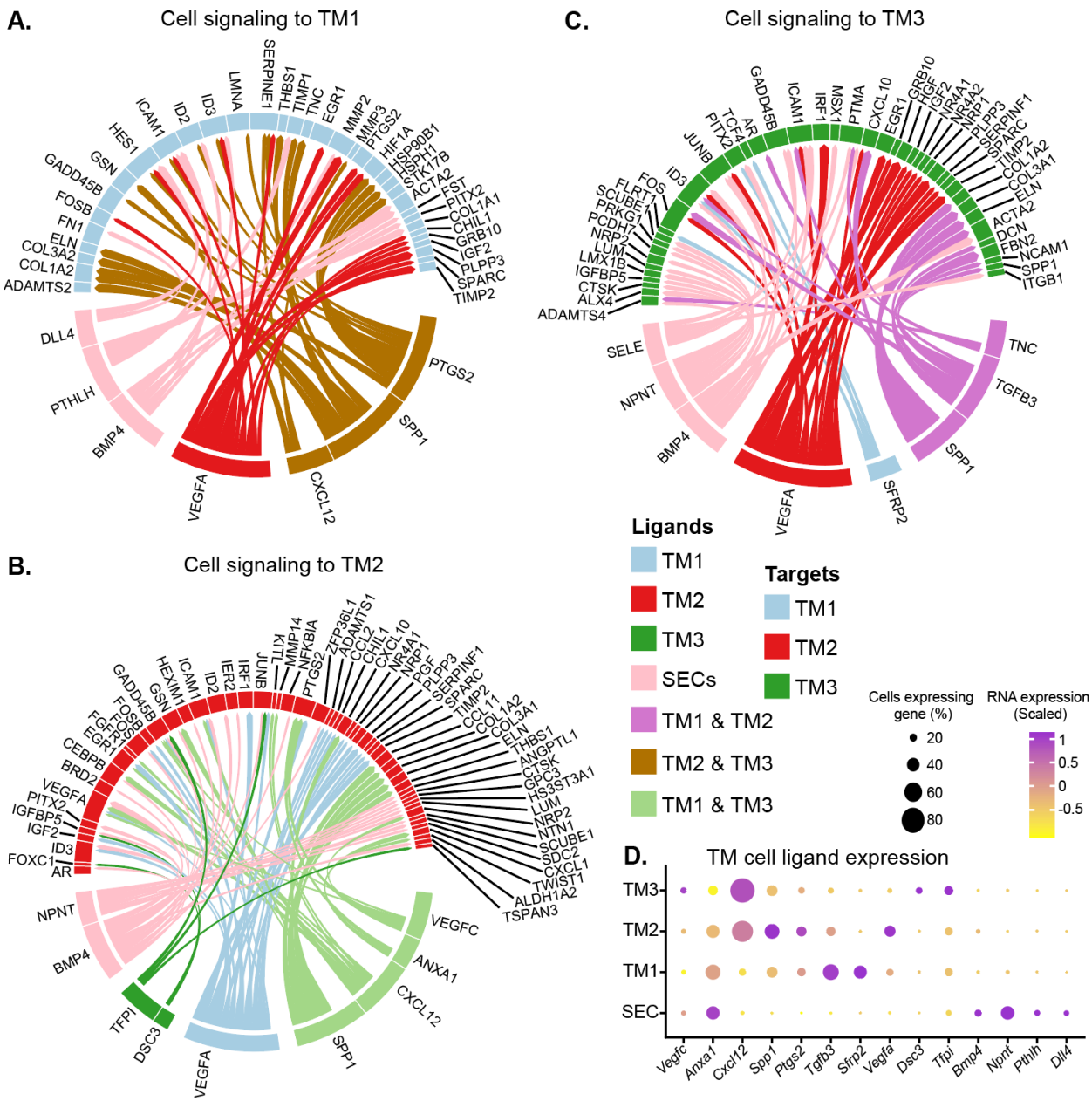

Supplemental Figure 11: TM-TM and SEC-TM signaling. (A-C) Analyses showing the top predicted interactions between TM and Schlemm's canal endothelial (SEC) ligands and individual TM cell target molecules (Circos plots). The three plots show target molecules in each individual TM cell subtype respectively. **(D)** The expression of all ligands predicted to have signaling interactions with TM cell subtypes (Dot plot).

Comparison to human TM cells

We next worked to relate our findings to human data. We compared marker genes for each of our TM cell subtypes to sequenced human TM cells from two previous studies (Patel et al.,

2020; van Zyl et al., 2020). These previous studies differed in the number of human TM cell subtypes that they reported and in the identities of their clusters. Van Zyl et al. identified three TM cell subtypes that they called JCT, beam A, and beam B (van Zyl et al., 2020), whereas Patel et al. identified two subtypes that they called fibroblast-like and myofibroblast-like (Patel et al., 2020). TM1 marker genes were most enriched in Van Zyl et al's human JCT cells (**Figure S12A**). Similarly, *Dcn* was expressed in mouse TM1 cells and was localized to fibroblast-like TM cells adjacent to SC by Patel et al. TM1 cell nuclei were typically shorter with greater sphericity than the elongated endothelial-like nuclei of TM3 cells (**Figure S13A-D**). This nuclear morphology was more consistent with a JCT than beam cell identity. Together, these data support a JCT identity for TM1 cells. TM2 cells were more closely related to human beam A and beam B cells than to the JCT cells reported by Van Zyl et al (**Figure S12B**). TM2 cells also shared expression of the *RSPO2* marker gene with the human myofibroblast-like cells reported by Patel et al. Together, this suggests that TM2 cells are myofibroblast-like beam cells. TM3 cells also shared marker genes with Patel et al's myofibroblast-like cells (*TAGLN* and *ACTA2*), suggesting TM3 cells are also beam cells. There was relatively equal TM3 marker gene enrichment across all human TM cell subtypes of Van Zyl et al (**Figure S12C**). Nuclei immediately adjacent to TM2 and TM3 cell marker staining had an elongated, endothelial-like shape (**Figure S13A-C**). This nuclear morphology was also consistent with the location of TM2 and TM3 cells on beams and analogous to the endothelial-like morphology of human beam cells (Stamer and Clark, 2017).

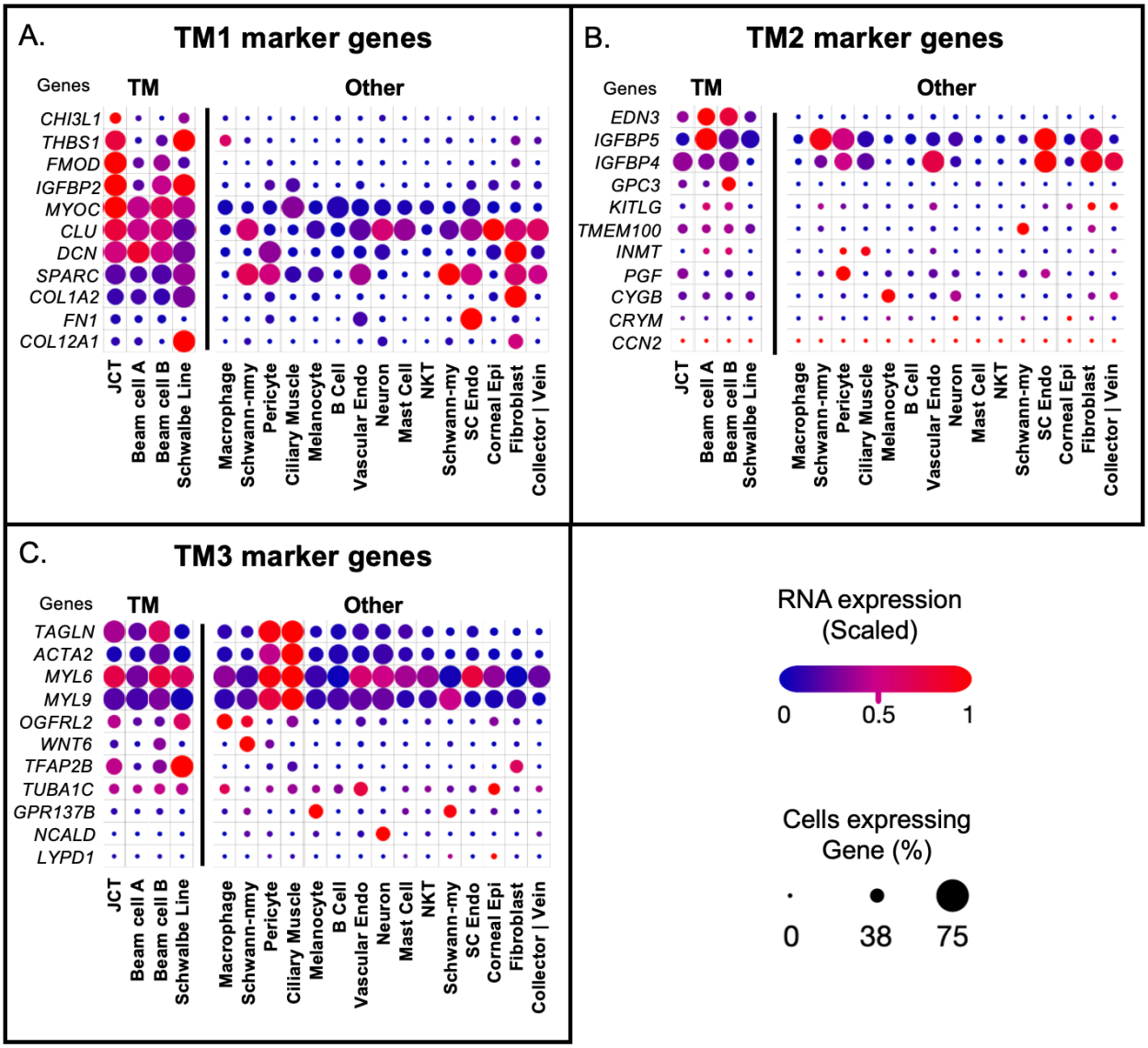

Supplemental Figure 12: Mouse TM subtype marker expression in human TM cells. (A-C) Dot plots of the expression of the top 11 marker genes for each of our mouse TM cell subtypes that have human orthologues expressed in the Van Zyl et al human dataset. TM1 marker genes generally have higher expression in the human JCT cluster than in any other cluster of cells. Other than EDN3, TM2 and TM3 marker genes do not show a strong enrichment for the annotated TM cells compared to other cells. Among TM cells, TM2 marker genes are more enriched in beam A and beam B cells. TM3 markers are mostly expressed in relatively equal levels across all the human TM cells. Schwalbe's line cells are also similar to TM. The anterior insertion of the TM is near Schwalbe's line, where TM stem cells are reported to reside. Therefore, the Schwalbe's line cells maybe TM stem cells.

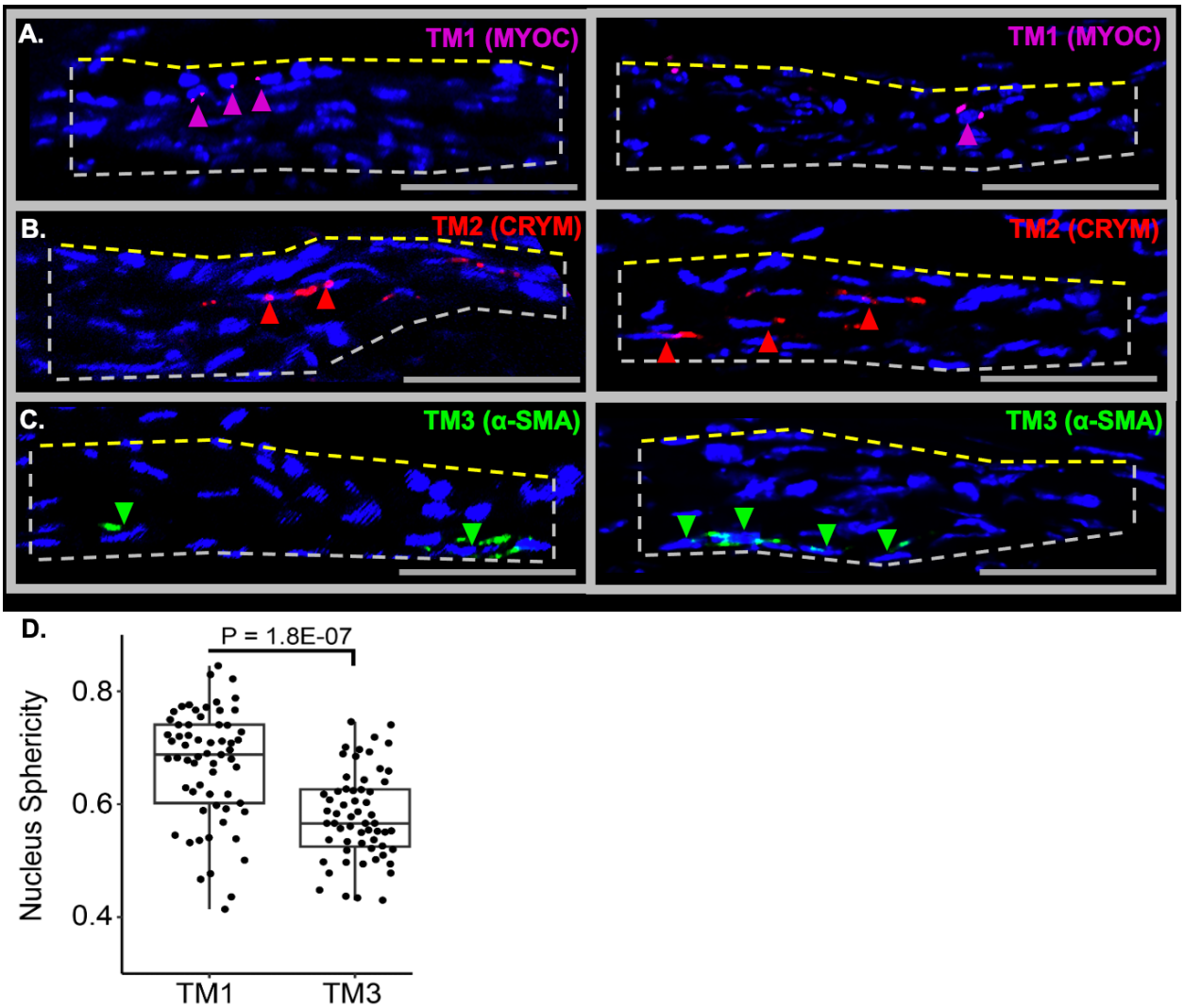

Supplemental Figure 13: Nuclear morphology of each TM subtype. (A-C) TM1 nuclei adjacent to the SC appear shorter than TM2 and TM3 nuclei and lack the typical elongated, endothelial-like morphology of beam cells. This shorter morphology gives TM1 nuclei a more spherical appearance. All scale bars: 50 μm. **(D)** To rigorously assess whether TM1 nuclei are more spherical, we analyzed their 3D shapes in whole mounts, comparing them to TM3 nuclei using the 'Sphericity' tool in Imaris. The data show that TM1 cells indeed have more spherical nuclei, consistent with a JCT identity. However, some TM1 cells exhibit more elongated nuclei, especially when located further from the SC. A higher sphericity score indicates a more rounded nucleus (with a completely spherical shape scoring 1. We characterized 60 randomly selected nuclei for each TM cell subtype. Groups were compared using Student's t-test.

Next, we evaluated the expression of genes implicated in elevated IOP and glaucoma by genome-wide association studies (GWAS). TM1 and TM2 cells had similar expression levels of GWAS genes associated with IOP elevation and primary open-angle glaucoma (POAG) respectively (**Figure S14A**). TM3 cells had slightly less expression of these GWAS genes

compared to TM1 and TM2. To better understand the genes driving GWAS gene enrichment in different TM subtypes, we studied pathways that are significantly enriched for GWAS genes **(Figure S14B-C,** see Table S6 for complete list). TM1 cells were the most enriched for genes involved in ECM organization, cell-substrate adhesion, and growth factor stimulus **(Figure S14D)**. All 3 TM subtypes had similar expression of GWAS genes associated with hormone stimulus, *Vegf* signaling, and *Rho* kinase signaling. TM3 cells expressed lipid and carbohydrate mitochondrial metabolism pathway genes at higher expression levels and in more cells than did TM1 and TM2 cells (**Figure S14E**). The same was true for actin binding-associated GWAS genes in TM3 cells versus TM1 and TM2. Genetic variation in lipid and carbohydrate mitochondrial metabolism pathways is associated with IOP elevation and glaucoma (Khawaja et al., 2016).

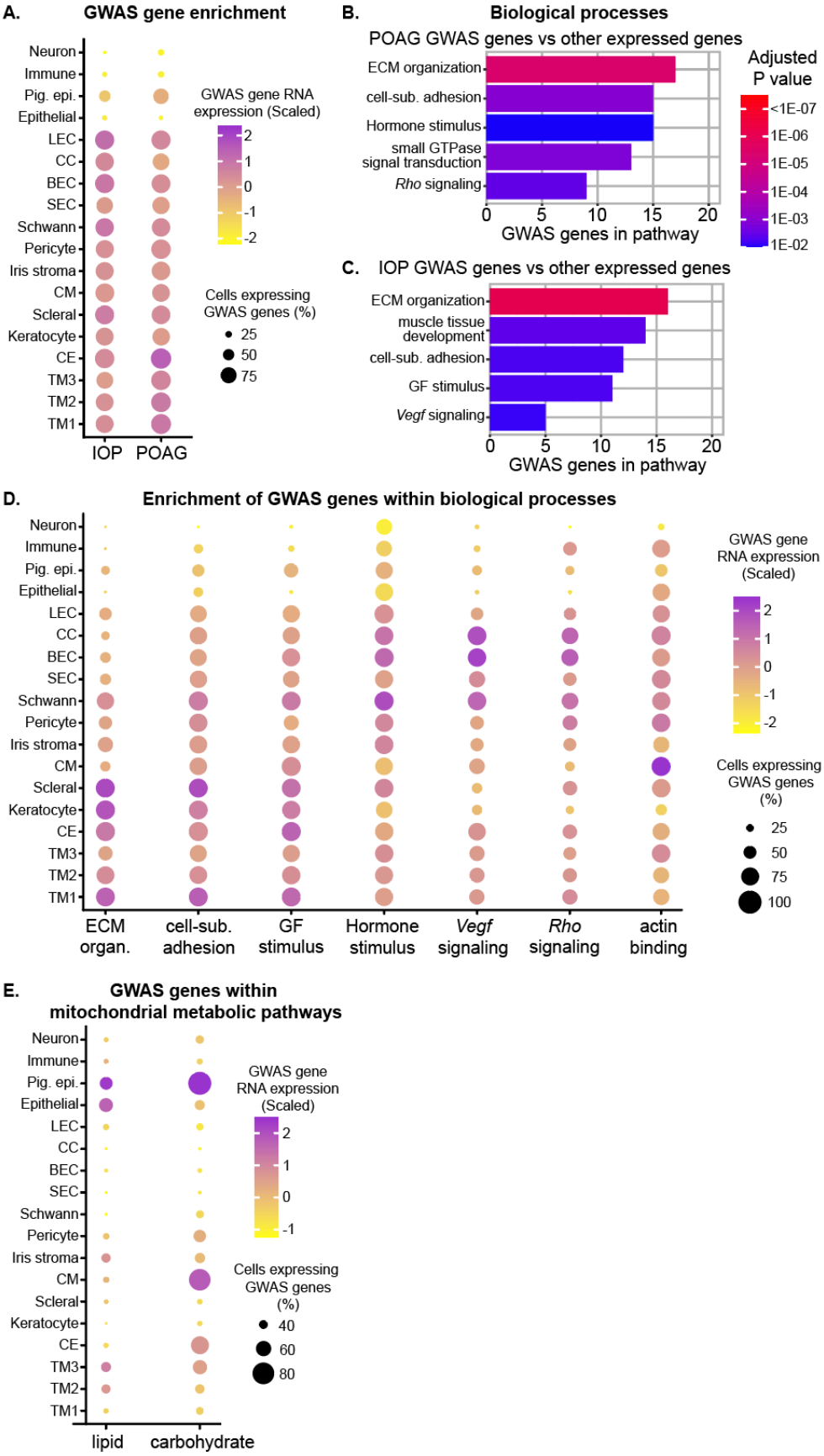
A.
GWAS gene enrichment
Neuron
Immune
Pig. epi.
Epithelial
LEC
CC
BEC
SEC
Schwann
Pericyte
Iris stroma
CM
Scleral
Keratocyte
CE
TM3
TM2
TM1
IOP
POAG
GWAS gene RNA expression (Scaled)
2
1
0
-1
-2
Cells expressing GWAS genes (%)
25
50
75
B.
Biological processes
POAG GWAS genes vs other expressed genes
ECM organization
cell-sub. adhesion
Hormone stimulus
small GTPase signal transduction
Rho signaling
0
5
10
15
20
GWAS genes in pathway
Adjusted P value
<1E-07
1E-06
1E-05
1E-04
1E-03
1E-02
C.
IOP GWAS genes vs other expressed genes
ECM organization
muscle tissue development
cell-sub. adhesion
GF stimulus
Vegf signaling
0
5
10
15
20
GWAS genes in pathway
D.
Enrichment of GWAS genes within biological processes
Neuron
Immune
Pig. epi.
Epithelial
LEC
CC
BEC
SEC
Schwann
Pericyte
Iris stroma
CM
Scleral
Keratocyte
CE
TM3
TM2
TM1
ECM organ.
cell-sub. adhesion
GF stimulus
Hormone stimulus
Vegf signaling
Rho signaling
actin binding
GWAS gene RNA expression (Scaled)
2
1
0
-1
-2
Cells expressing GWAS genes (%)
25
50
75
100
E.
GWAS genes within mitochondrial metabolic pathways
Neuron
Immune
Pig. epi.
Epithelial
LEC
CC
BEC
SEC
Schwann
Pericyte
Iris stroma
CM
Scleral
Keratocyte
CE
TM3
TM2
TM1
lipid
carbohydrate
GWAS gene RNA expression (Scaled)
2
1
0
-1
Cells expressing GWAS genes (%)
40
60
80

Supplemental Figure 14: GWAS gene expression in limbal cells. (A) Expression of genes implicated in risk for IOP elevation (left) and primary open-angle glaucoma (POAG, right) in humans GWAS plotted against mouse limbal cell type. There is similar GWAS gene expression across TM cell subtypes and other limbal cell types. TM1 and TM2 have a slightly higher expression of GWAS genes compared to TM3. **(B-C)** Pathway analysis (Gene ontology, GO) shows enrichment of biological pathways for the POAG (B) or IOP (C) genes vs other expressed genes considering all cell types (see Table S6 for full list of GWAS gene-enriched pathways). **(D)** Enriched biological pathways among POAG GWAS genes within the indicated cell types. **(E)** Cell type enrichment of lipid and carbohydrate metabolism pathway genes that are significantly associated with POAG (Khawaja et al.). ECM organ. = extracellular matrix organization, cell-sub. = cell-substrate adhesion, Hormone stimulus = cellular response to hormone stimulus, small GTPase signal transduction = regulation of small GTPase mediated signal transduction, *Rho* signaling = regulation of Rho protein signal transduction, GF stimulus = regulation of cellular response to growth factor stimulus, *Vegf* signaling = vascular endothelial growth factor receptor signaling pathway.

Regulation of TM cell gene expression

To better understand the overlap and differences in transcriptional control of TM cell gene expression, we performed single-cell resolution multiome sequencing. Using limbal strip tissue isolated from a separate cohort of mice than those used for scRNA-seq, we simultaneously performed both single nucleus RNA sequencing (snRNA-seq) and snATAC-seq. We thus captured both gene expression and open chromatin data throughout the genome in the same cell. Using the snRNA-seq data, we clustered cells into various cell types. The generated clusters and their marker genes closely agreed with our scRNA-seq analyses (**Figure 5A-B, Figure S15A**). Notably, there was a significant correlation between gene expression (RNA-based clustering) and chromatin accessibility (ATAC-based clustering) with adjusted Rand index of 0.20 ($p < 0.001$, permutation test, **Figure S15B-D**). This included an increase in chromatin accessibility at the promoters of marker genes in their respective TM cell subtypes (**Figure 5C-E**). To discover the key transcriptional regulators within TM cells, we examined the correlation between the expression of each transcription factor (TF) and their chromatin accessibility at predicted binding sites within all TM cells. Various TFs that either activated or repressed transcriptional activity exhibited good correlations with gene expression across TM cells (**Figure 5F**). Such activating TFs include *Tcf21*, *Arid3b*, and *Myc*, while repressing TFs include *Meox2*, *Junb*, and *Sox6*. Notably, *LMX1B*, an important gene in glaucoma GWAS (Choquet et al., 2018; Gao et al., 2018; Gharahkhani et al., 2021; Khawaja et al., 2018; MacGregor et al., 2018; Shiga et al., 2018), is among the most strongly activating TFs in TM cells.

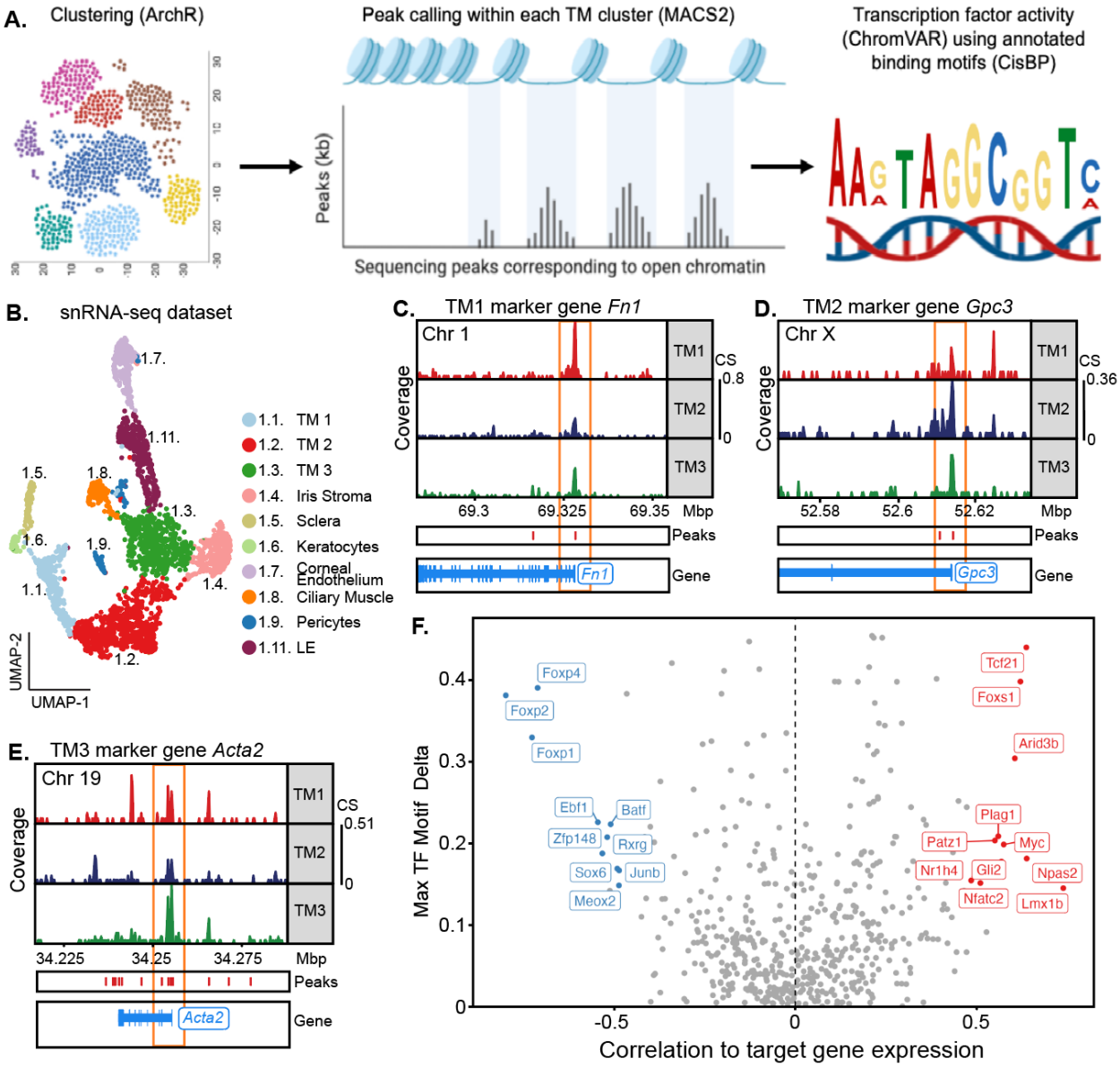

Figure 5: Transcription factors dictating gene expression in TM cells (A) A schematic representation of the pipeline used to identify open chromatin sites and active transcription factors (TFs). Individual cells were profiled using both single nucleus (sn) RNA and ATAC sequencing (multiome). TM cell clusters were identified using the snRNA-seq data, while significantly open chromatin regions were identified using the snATAC-seq data. Active TFs were determined based on the odds ratio of TF binding motifs within these open chromatin regions. Schematic created with BioRender.com **(B)** UMAP of subclusters derived from TM cell containing cluster (cluster 1) in the snRNA-seq data. **(C-E)** Example ATAC tracts for the promotor regions of selected marker genes for TM1 (C), TM2 (D), and TM3 (E). Each of these marker genes has greater promoter accessibility in the TM cell subtype in which its RNA expression is enriched (orange box). The aligned marker gene positions are shown. Coverage = normalized ATAC signal reads in transcription start site. CS = coverage scale. **(F)** Correlations between RNA expression levels (snRNA-seq dataset) of each TF and the chromatin accessibility levels (snATAC-seq dataset) of their respective predicted target binding motifs

across all TM cell subtypes (see Methods). Select TFs with strong positive (red) or negative correlations (blue) are named.

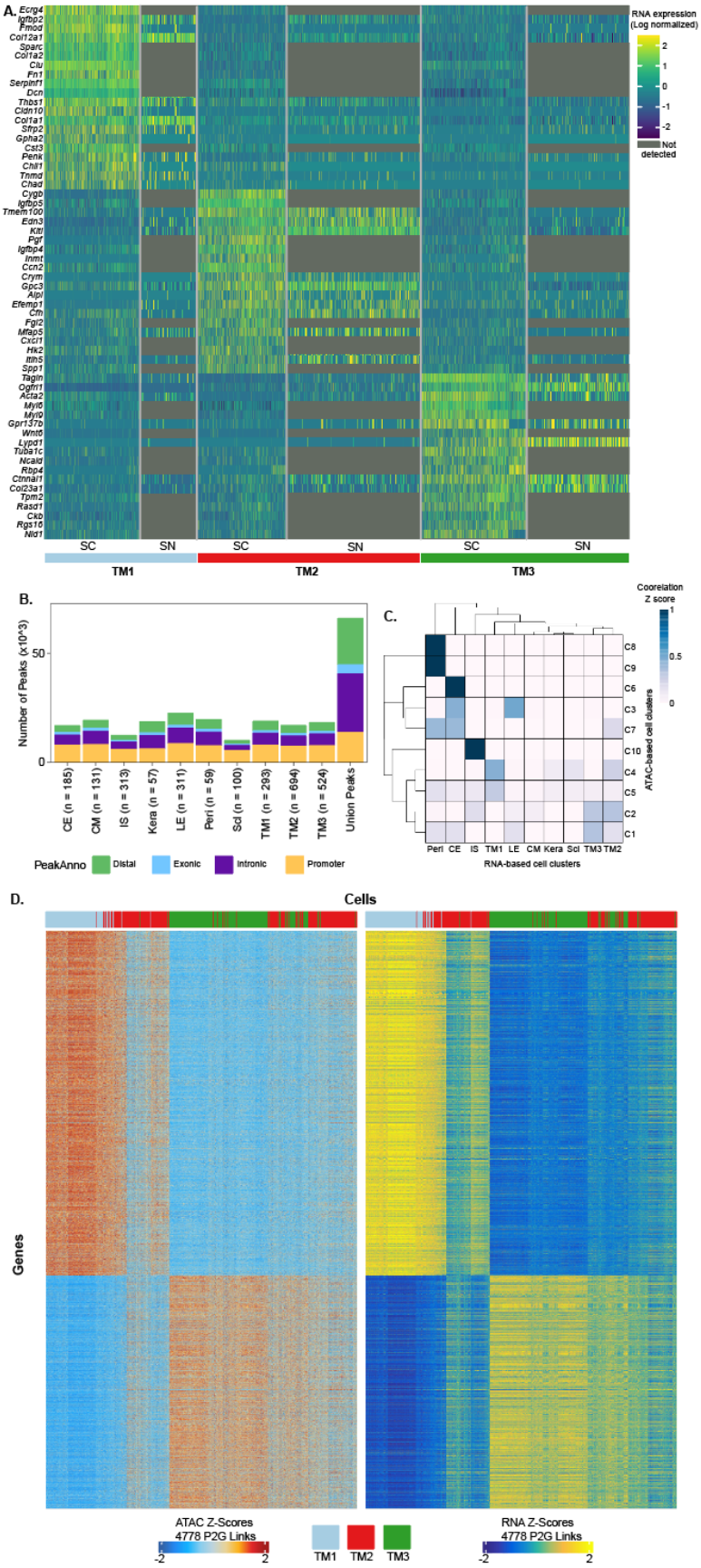
A.
RNA expression (Log normalized)
Not detected
SC
SN
TM1
TM2
TM3
B.
Number of Peaks (x10^3)
CE (n = 185)
CM (n = 131)
IS (n = 313)
Kera (n = 57)
LE (n = 311)
Peri (n = 59)
Scl (n = 100)
TM1 (n = 293)
TM2 (n = 694)
TM3 (n = 524)
Union Peaks
PeakAnno
Distal
Exonic
Intronic
Promoter
C.
Coorelation Z score
ATAC-based cell clusters
RNA-based cell clusters
D.
Cells
Genes
ATAC Z-Scores 4778 P2G Links
RNA Z-Scores 4778 P2G Links

Supplemental Figure 15: Analysis of ATAC dataset (A) Overlap of marker gene expression for each TM cell subtype between single-cell (sc) and single-nucleus (sn) RNA sequencing (RNA-seq). Other than the expected technical drop out of genes (no detected expression) in the snRNA-seq dataset, there is good agreement. **(B)** Localization of significantly open chromatin regions (snATAC-seq). **(C)** Confusion matrix of clusters identified by snRNA-seq and snATAC-seq after separately clustering each data type using unbiased dimensional reduction. There is a significant correlation between gene expression (RNA-based clustering) and chromatin accessibility (ATAC-based clustering) with adjusted Rand index of 0.20 ($p < 0.001$, permutation test). **(D)** Heatmaps comparing the open chromatin score at a gene promoter (left panel, snATAC-seq) to the RNA expression (right panel, snRNA-seq). Individual genes are represented on the y-axis and individual cells are plotted on the x-axis (only TM cells included). The consistent heatmap patterns indicate a strong overlap between promoter chromatin states and RNA expression for individual genes across cell types, validating the quality of these multiome datasets.

Metabolism-supporting treatment lessens IOP elevation in *Lmx1b*^{V265D} mice

We evaluated the utility of our new TM cell atlas to better understand the functions of *Lmx1b* in TM cells and how *Lmx1b* mutations lead to glaucoma. To do this, we analyzed scRNA-seq data generated for limbal cells from mice with a dominant mutation in *Lmx1b* (*Lmx1b*$^{V265D/+}$). These mutant C57BL/6J mice develop early onset IOP elevation (Cross et al., 2014; Tolman et al., 2021; Zhang et al., 2024). We compared gene expression in *V265D* mutant TM cells after integration with our wild-type data (all data B6 background and postnatal day 60, **Figure 6A**, **Figure S16A**). Results show that *Lmx1b* is minimally expressed in TM1 and TM2 but is highly expressed in TM3 cells (**Figure 6B**). Next, we analyzed DEGs and pathway differences between WT and *V265D/+* cells across each TM cell subtype. Across all TM subtypes, various genes related to ECM function and growth factor signaling were downregulated in mutants, including glycosaminoglycans and insulin growth factor binding proteins (**Figure 6C**, **Table S6** for complete list of pathways). Pathways enriched in mutant TM cells were associated with ribosome and calcium signaling. We then examined the differential responses to the *Lmx1b* mutation by analyzing pathways dysregulated in each TM subtype that were not common across all TM cells (**Figure 6D-F**, **Figure S16B**). *V265D* mutant TM1 cells had a downregulation of collagen synthesis/metabolism gene expression relative to WT cells, particularly in the production and turnover of fibrillar collagens. TM2 cells with *Lmx1b* mutations had upregulation of immune signaling pathways. The highly *Lmx1b* expressing TM3 cells exhibited perturbed mitochondrial metabolism, with a downregulation of genes in complex I and ATP synthase, and upregulation of genes involved in ubiquitin pathways. These results document altered mitochondrial function and proteostasis in TM3 cells.

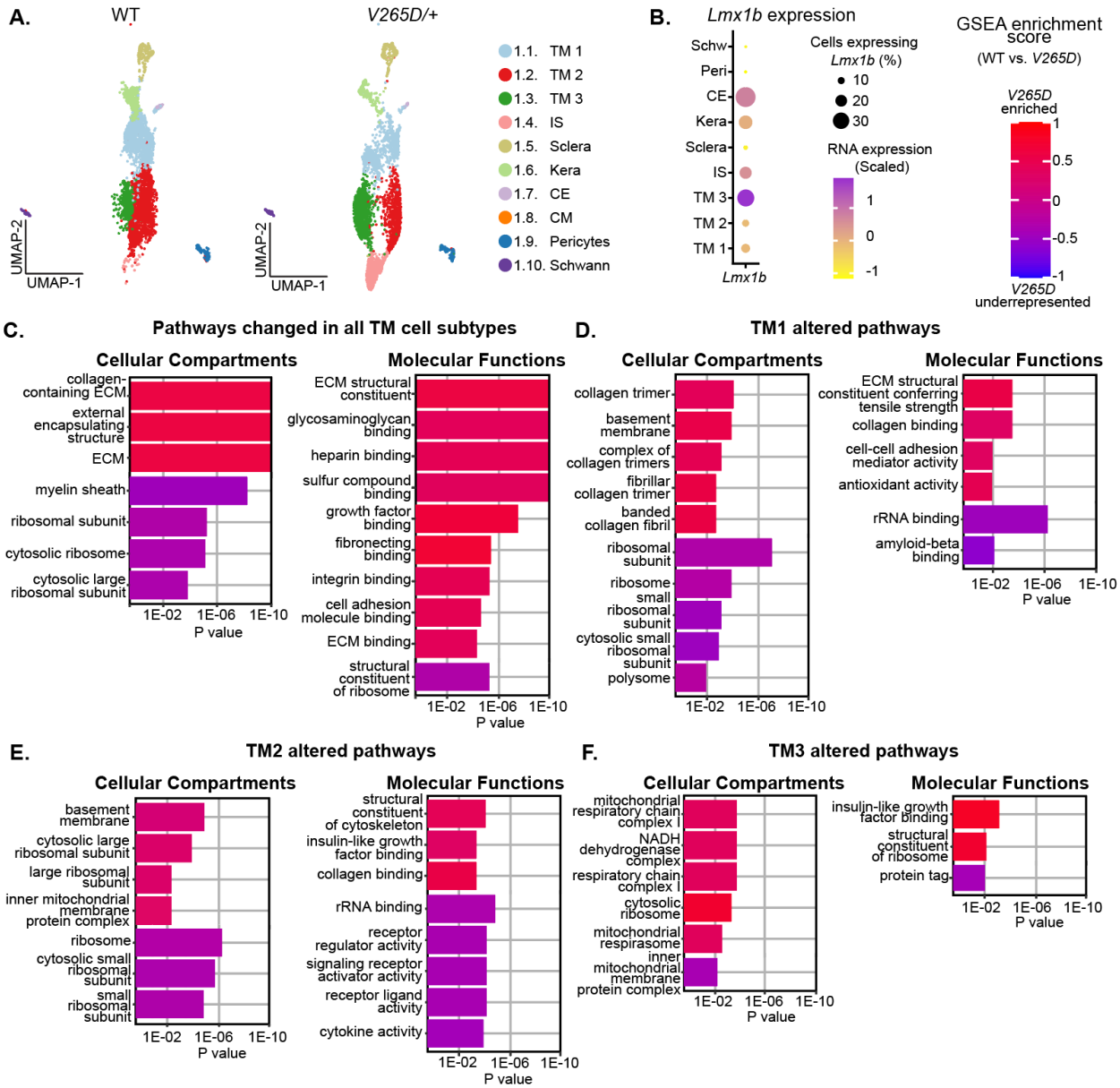

Figure 6: Differential molecular responses of TM cell subtypes to an *Lmx1b* mutation (A) UMAPs of limbal cells from WT and *Lmx1b*$^{V265D/+}$ (*V265D*) mutant mice (both genotypes B6 background). **(B)** *Lmx1b* expression across limbal cell types. *Lmx1b* expression is highest in TM3 cells. **(C)** Pathways that are changed in all TM cell subtypes. **(D-F)** Top pathways that are significantly altered when comparing each indicated TM cell subtype across genotypes. Many of these pathways were not significantly changed when comparing all TM cell subtypes as a group, indicating that the *V265D*-induced changes are strongest within each TM cell subtype. *V265D* has a pronounced effect on mitochondrial pathways in TM3 cells but much less so in other TM cells. ECM = extracellular matrix. ECS = extracellular structure.

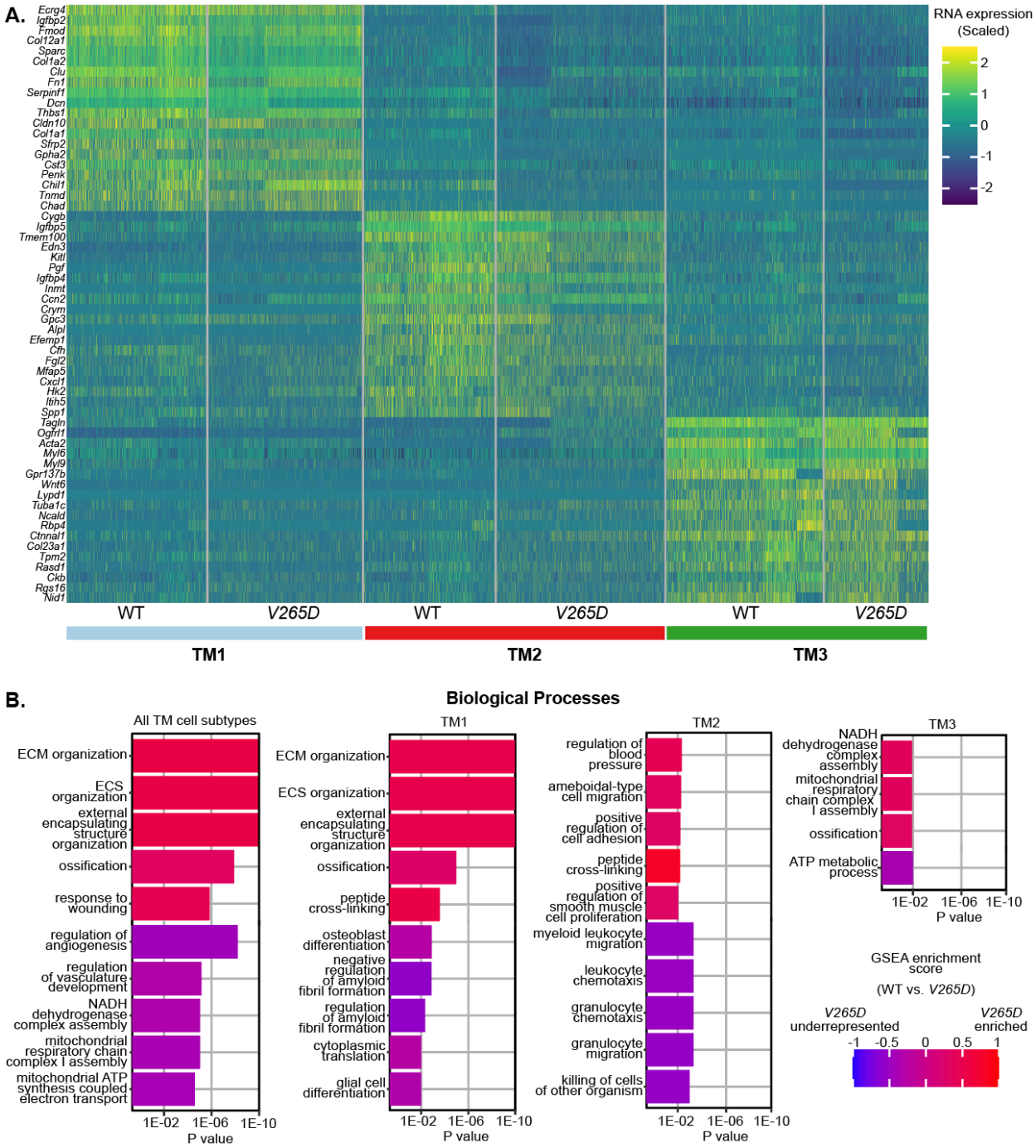

Supplemental Figure 16: Further pathway analyses of *Lmx1b*^{V265D} vs WT. (A) Heatmaps comparing marker genes for all TM cell subtypes across genotype. **(B)** The top 10 *V265D* upregulated and downregulated biological processes for the indicated comparisons across genotype are shown (all scRNA-seq data, Adjusted P values, axis cut of at 1E-10). ECM = extracellular matrix. ECS = extracellular structure.

Our findings implicated perturbed metabolism within TM3 cells as responsible for IOP elevation in an *Lmx1b* glaucoma model. Nicotinamide (NAM) is known to boost nicotinamide adenine dinucleotide (NAD), supporting healthy metabolism/ mitochondrial function (Schondorf et al., 2018; Williams et al., 2017b). Thus, we hypothesized that the metabolic abnormalities in TM3 cells underlie the IOP elevation that causes glaucoma, and that NAM treatment may protect the *Lmx1b* mutant TM. Beyond *LMX1B*, this hypothesis is relevant more commonly to POAG treatment because metabolism-relevant genes are implicated by GWAS (and their expression is enriched in TM3 cells, **Figure S14E**). To test our hypothesis, we treated mice by adding NAM to their drinking water starting at postnatal day 2 and continuing into adulthood. Results showed that NAM supplementation significantly protected against anterior chamber deepening (ACD, a symptom of IOP elevation, **Figure 7A-B**) and IOP elevation (**Figure 7C-D).** These results support NAM as a treatment to prevent TM damage and IOP elevation in LMX1B-mediated glaucoma with potential general relevance to POAG.

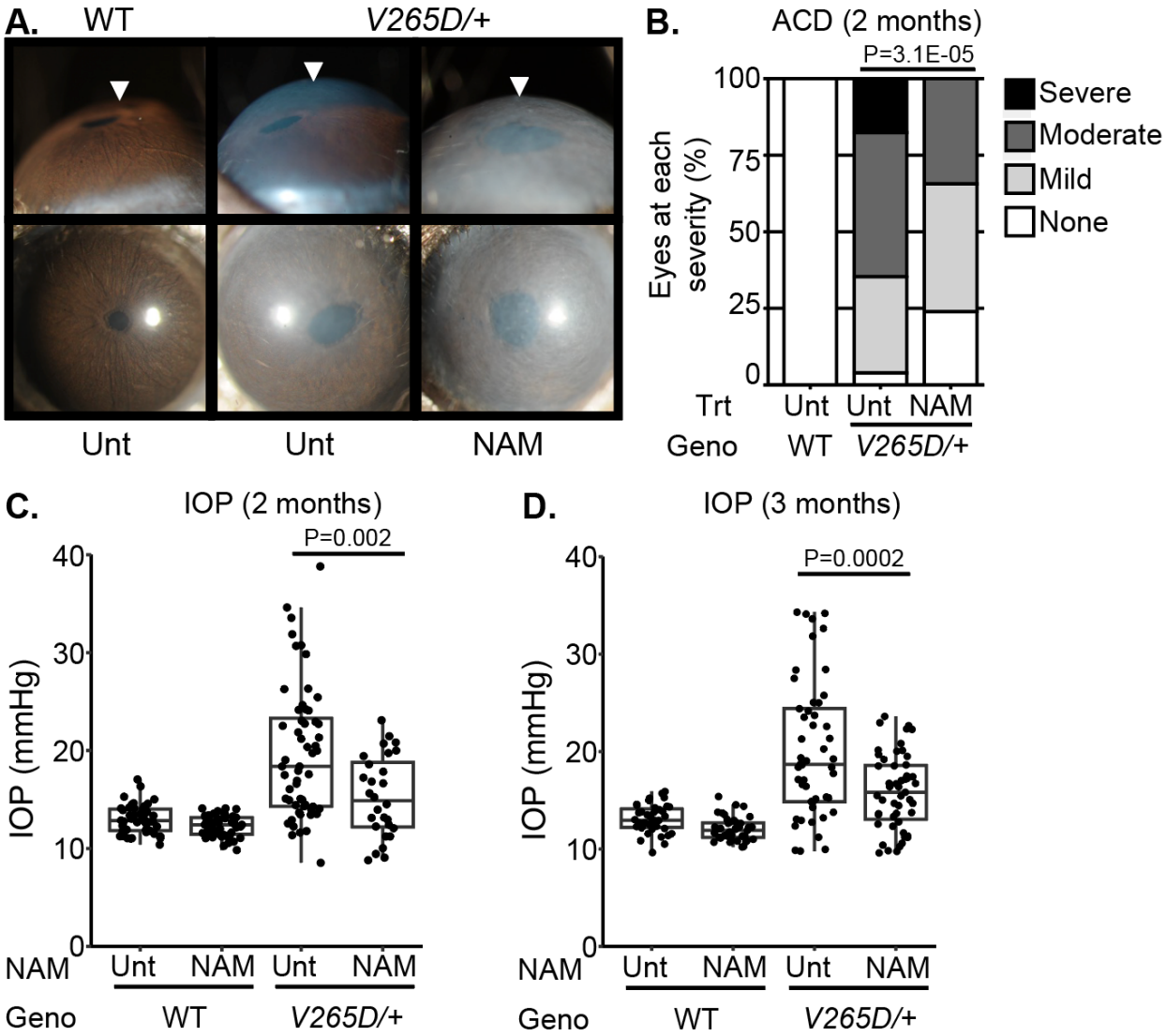

Figure 7: Nicotinamide treatment protects from IOP elevation in *Lmx1b* mutants. (A) Representative photos of eyes from mice of the indicated genotypes and treatments (UNT = untreated, NAM = nicotinamide treated, 550mg/kg/day provided in drinking water). NAM treatment substantially lessens anterior chamber deepening (ACD), a sensitive indicator of IOP elevation in mice. The WT and NAM-treated mutant eyes have very shallow anterior chambers while the untreated mutant eye has an obviously deepened chamber (arrowheads). **(B)** Distributions of anterior chamber depth based on previously defined scoring system (Tolman et al., 2021). Groups compared by Fisher's exact test. **(C-D)** Boxplots of IOP (interquartile range and median line) in WT and mutant eyes of both NAM treated and untreated groups. NAM treatment significantly lessens IOP elevation in mutants compared to untreated mutant controls. Groups compared by Two-way ANOVA followed by Tukey's Honestly significant difference. Geno = genotype.

Discussion

This study provides a comprehensive multimodal analysis of mouse limbal cells that focuses on the TM. We defined three TM cell subtypes with unique marker panels that can be used for their identification across different strains, laboratories, and processing methods. We validated key marker gene expression by IF and ISH, discovering biases for specific TM subtypes to reside in different parts of the TM. For example, TM1 cells have a location bias for the outer, posterior TM while TM3 cells are more abundant in the inner, anterior TM. Importantly, our pathway analyses suggest that the different TM subtypes have overlapping roles. All 3 TM subtypes are enriched in ECM synthesis and ECM metabolism compared to other limbal subtypes. However, there is also compartmentalized enrichment of some processes to specific subtypes. For example, ECM production and turnover, secreted ligand signaling, debris removal, immune surveillance, actin-associated cell contraction and increased metabolic gene activity (as discussed below) are enriched in specific cell-subtypes. Using ATAC-seq data, we discovered key transcription factors controlling gene expression in TM cells, including LMX1B. Importantly, we implicate LMX1B in metabolic control in TM cells. More specifically, we demonstrate that *Lmx1b* is most active in TM3 cells, while mutation of *Lmx1b* induces prominent mitochondrial defects in TM3 cells. Finally, we show that therapeutically targeting TM3 dysfunction with a mitochondrial/ metabolism supporting nutrient (nicotinamide) protects from IOP elevation in the *Lmx1b* glaucoma model. We also suggest that a TM3-like cell is generally relevant to metabolic pathways in human glaucoma based on enriched expression of human glaucoma GWAS gene in TM3 cells. Together these data provide a wealth of new molecular information about TM cells and suggest a new approach for preventing IOP elevation.

Mouse trabecular meshwork subtype classification

Here we provide evidence for three TM cell subtypes in mice that are robust across datasets from different institutions, using different tissue processing and sequencing protocols. Although others (Thomson et al., 2021; Ujiie et al., 2023) subdivided TM cell subtypes beyond the three defined in the present study, at this point we decided against further subdivision (See Figure S5) for the following reasons. We lacked confidence in the higher resolution clustering, as it was not consistent across datasets, did not produce unique marker gene sets, and could have resulted in over-clustering due to stochastic or stress-induced differences between subpopulations of cells. Moreover, the number of reported mouse TM cell clusters in previous studies were

inconsistent. Although three TM subtypes were reported by Van Zyl et al. and Ujiie et al. (Ujiie et al., 2023; van Zyl et al., 2020), the molecular features of cells in these clusters were not the same across these studies. Differences between studies may be due to batch effects, different computational methods and possibly over-clustering. Most importantly, there was very limited validation by IF, IHC, or other methods in previous studies. Only the JCT type of TM cell in these previous studies was assessed by means other than scRNA-seq (IF and ISH, van Zyl et al., 2020). Additionally, Thompson et al. treated cells with Y27632, a ROCK inhibitor, which could alter TM cell transcriptomes. It is also important to point out that both Thompson et al. and Van Zyl et al. used albino mouse strains, which can impact TM cell development and function (Libby et al., 2003). Finally, Ujiie et al. sequenced TM cells at 3-4 weeks, which is prior to full maturation of the TM structure (Smith et al., 2001),zsadxz
\"¿ while our ongoing developmental studies show substantial molecular maturation of TM cells between P21 and P60.

As Van Zyl et al's data is deposited in the Broad Institute's single-cell portal, we further compared their data with ours. Although both Van Zyl et al. and our current paper identified 3 TM subtypes, our work does not fully agree. Some of the cells named beam A and beam Y by Van Zyl et al. express markers present in our TM2 cell subtype, while others express markers that are absent in TM2 cells but present in our scleral cells. Our IF studies confirm that these discordant markers are not expressed in TM cells, but instead show that they are in fact scleral cells. These scleral cells highly express fibroblast markers including *Mfap5*, *Clec3b*, and *Tnxb*, suggesting they are scleral fibroblasts. Cells initially named uveal cells by Van Zyl et al. (and subsequently by Ujiie et al. and Thompson et al.) express markers of our TM3 cells. Consistent with our gene expression data, our IF shows that these Van Zyl markers are expressed by cells that are primarily located in the TM region that is closer to the cornea and not in the uvea or the TM region adjacent to the uvea. Thus, our current study resolves some previous inconsistencies in classifying mouse TM cell subtypes. It lays a firmer foundation for continued understanding of TM cell types and their biology. Moving ahead, sequencing cells at greater depths will enhance TM cell characterization and improve comparisons between datasets.

Differential roles of specific mouse TM cell subtypes and comparison to human

As a group, all TM cells share various molecular properties that distinguish them from other ocular cells. Our analyses determine the expression of IOP, and glaucoma genes identified by

GWAS in TM cell subtypes as well as in other limbal cells. Pathways enriched across all TM cell subtypes based on RNA-seq are largely related to ECM (including collagens, integrins, and glycosaminoglycan pathways), cell-cell signaling, and growth factor signaling. This fits with an essential role of the TM in both ECM synthesis/turnover and in signaling to the SC to maintain IOP (Balasubramanian et al., 2024; Fuchshofer and Tamm, 2009; Keller et al., 2009; Stamer and Acott, 2012; Thomson et al., 2021). Additionally, genes associated with intermediate filaments, which function in determining cell shape and structure and can also act as mechanical stress absorbers (Herrmann et al., 2007), are underrepresented in TM cells. Lower levels of intermediate filaments may enable TM cells to alter their shape to respond to changes in IOP.

Mouse TM1 cells closely resemble sequenced human JCT cells. Like human JCT cells, the majority of TM1 cells are located nearest to the SC inner wall, particularly adjacent to the posterior of the mouse SC. Human JCT cells are generally accepted to be embedded in a more diffuse ECM and to not cover the collagenous trabecular beams (Keller and Acott, 2013; Stamer and Clark, 2017; Vranka et al., 2015). In vivo, a proportion of TM1 cells have a shorter, more spherical nuclear morphology, consistent with JCT cell identity. Importantly, the JCT region is critical in determining resistance to AH outflow and in regulating IOP (Acott and Kelley, 2008; Ethier, 2002; Johnson, 2006; Stamer and Acott, 2012). JCT cells have fibroblast-like properties, including the secretion of ECM proteins and degradation enzymes to support continuous ECM remodeling (Acott et al., 1988; Keller et al., 2009; Stamer and Clark, 2017). The subset of TM1 cells that lie distant from SC have more beam cell-like, elongated nuclear morphology. This suggests that either our TM1 cluster contains more than 1 TM cell subtype or that the morphology of a single TM1 cell subtype is influenced by local environment. This needs to be resolved by future studies. Compared to the other TM cell subtypes, TM1 cell pathways are enriched in both ECM structural molecules, such as collagens and integrins, and TGF-β signaling, which increases ECM production (Munger and Sheppard, 2011). Notably, excessive TGF-β signaling and ECM production can lead to fibrosis and elevate IOP (Biernacka et al., 2011; Frangogiannis, 2020; Meng et al., 2016). These data suggest that TM1 cells play an important role in the constant remodeling of the ECM. However, dysregulation of these pathways can be pathogenic.

TM2 cells molecularly resemble previously sequenced human TM beam cells (Patel et al., 2020; van Zyl et al., 2020). This includes overlap of expression of top TM2 signature gene expression

with sequenced human beam cells. Consistent with a beam cell identity, TM2 cells are located more towards the mid and inner TM than most TM1 cells. TM2 cells have an elongated nuclear morphology, consistent with the previously established beam cell morphology of cells in the regions they occupy (Overby et al., 2014; Smith et al., 2001; Stamer and Clark, 2017). Beam cells have endothelial-like properties, such as maintaining the patency of the AH outflow tract through the production of antithrombotic molecules. Proteases and molecules classically known as antithrombotic and thrombolytic maintain fluid flow through the TM by preventing build-up of protein aggregates to maintain fluid drainage (Acott and Kelley, 2008; Stamer and Acott, 2012). Such molecules include glycosaminoglycans, like heparin, the serine protease tPA and matrix metalloprotease that are all highly expressed in TM2 cells. Beam cells are also phagocytic and this activity along with turnover of ECM further cleans the TM (called filtering) to enhance fluid drainage (Stamer and Clark, 2017). Human Beam cells also participate in antigen presentation and modulation of inflammation through cytokines and major histocompatibility proteins (Shifera et al., 2010; Stamer and Clark, 2017), consistent with TM2 cells being enriched for these immune pathways/ molecules. Additionally, our data suggest that signaling from TM2 cells to SC endothelial cells is mediated by soluble molecules including *Vegfa*, *Edn3*, and *Angpt1*, which are critical for SC maintenance and function. This links TM2 cells to ocular development and glaucoma. VEGF receptor and ANGPT signaling genes modulate SC development/ function as well as contribute to developmental and primary open-angle glaucoma (Aspelund et al., 2014; Kabra et al., 2017; Khawaja et al., 2018; Kizhatil et al., 2014; MacGregor et al., 2018; Souma et al., 2016; Thomson et al., 2020).

TM3 cells also have a location and elongated nuclear morphology resembling beam cells with enriched localization in the inner, anterior TM. TM3 cell-enriched processes include actin binding, and modulation of the actomyosin system, which is known to modulate outflow resistance and IOP (Rao et al., 2001; Yu et al., 2008). As such, TM3 cells express a large percentage of glaucoma-associated genes involved in actin binding at a high level. Importantly, TM3 cells are enriched for various mitochondrial metabolic and antioxidant pathways, including those associated with IOP elevation and glaucoma (Aboobakar et al., 2023; Khawaja et al., 2016). Inhibiting metabolic pathways alters AH outflow resistance (Reina-Torres et al., 2020). Since maintaining contractile tone is an energy-intensive process (DeWane et al., 2021), this could explain the enrichment of energy metabolism pathways in TM3 cells compared to other TM cells.

TM3 cells have a unique susceptibility to mitochondrial dysfunction

In addition to being enriched in mitochondrial/ energy metabolism processes, TM3 cells express *Lmx1b* at significantly higher levels than both the other TM cell subtypes and other limbal cells. Importantly, in heterozygous mutant *V265D/+* mice, TM3 cells had pronounced gene expression changes that implicate mitochondrial dysfunction and oxidative stress, but that were absent or much lower in other cells including TM1 and TM2. Together, these data suggest that mutation of *Lmx1b* has a primary effect on metabolism and oxidative stress in TM3 cells that subsequently leads to IOP elevation and then glaucoma. Relevantly, homozygous conditional knockout of both *Lmx1b* and *Lmx1a* as well as siRNA knockdown of *Lmx1b* alone impact mitochondrial functions in neurons and may contribute to Parkinson's disease (Bergman et al., 2009; Doucet-Beaupre et al., 2016; Jimenez-Moreno et al., 2023). Our data extend these published findings by showing that inheritance of a single dominant mutation in *Lmx1b* similarly affects metabolism in TM3 cells. In addition to modulating mitochondria, LMX1B was recently identified as a transcription factor that regulates responses to cell stress. This includes promotion of autophagy under stress conditions to enable recycling of cellular resources to maintain cellular functions and enable survival (Jimenez-Moreno et al., 2023). Thus, mutation of *Lmx1b* may also result in a deficiency of the beneficial autophagic response to stress (Jimenez-Moreno et al., 2023). Although further experiments are needed, dysfunctional autophagy may further prolong and exacerbate TM cell stress, resulting in more extensive depletion of cellular resources, exacerbated cellular dysfunction, and IOP elevation. Other consequences of the *Lmx1b* mutation that were evident in the *V265D/+* cells may also contribute to IOP elevation, including the overexpression of genes associated with ribosomes and calcium signaling, and depletion of genes involved with ECM synthesis and metabolism. However, these processes were not limited to TM3 cells or even to cell types that express detectable *Lmx1b*, suggesting that they are secondary damaging processes that are subsequent to the initiating, *Lmx1b*-induced, metabolic disturbances and cell stress in TM3 cells. Thus, we hypothesize that mitochondrial abnormalities in TM3 cells are of primary importance to IOP elevation in *V265D/+* glaucomatous mice.

Nicotinamide protects against IOP elevation in *Lmx1b*^{V265D}-mutant mice

Based on our findings in TM3 cells, we tested if mitochondrial and metabolic disturbances are important in IOP elevation by administering nicotinamide (NAM). NAM is a form of vitamin B3

that is well-established to boost NAD^+ levels, promote mitochondrial health and energy metabolism, relieve oxidative stress and thus promote cellular resilience (Gomes et al., 2013; Imai and Guarente, 2014; Jang et al., 2012; Mouchiroud et al., 2013; Verdin, 2015; Williams et al., 2017b, Jang et al., 2012; Kang and Hwang, 2009; Song et al., 2021). Supporting our hypothesis of primary metabolic dysfunction in TM3 cells, NAM treatment strongly protected *V265D/+* mice from IOP elevation. Thus, treatments that support normal metabolism may protect from IOP elevation in individuals with *LMX1B* variants including both developmental glaucoma and POAG patients (Chen et al., 1998; Choquet et al., 2018; Choquet et al., 2017; Gao et al., 2018; Gharahkhani et al., 2021; Khawaja et al., 2018; MacGregor et al., 2018; Sweeney et al., 2003; Vollrath et al., 1998). As NAM and other NAD^+ boosting treatments are also known to be directly neuroprotective in glaucoma (De Moraes et al., 2022; Hui et al., 2020; Williams et al., 2018; Williams et al., 2017a; Williams et al., 2017b), our current data suggest that such treatments will have a double benefit for patients. As mitochondrial defects are becoming broadly associated with glaucoma risk and progression (Abu-Amero et al., 2006; Lo Faro et al., 2021; Petriti et al., 2024)**,** these treatments could have wide-ranging potential to complement and augment existing IOP-lowering therapeutics through a completely distinct mechanism.

Our results provide a thorough molecular characterization of mouse TM cells, providing much needed molecular information on subtype specializations in regulating IOP and the roles of specific subtypes in glaucoma. This comprehensive TM atlas provides a new foundation to guide development of new glaucoma treatments. We validate its utility by implicating metabolic changes in a single TM cell subtype in both mouse and human glaucoma, with success of a metabolic treatment targeting this subtype in a glaucoma model.

Methods

Animal husbandry and ethics statement

Experimental animals were either C57BL/6J (Stock# 664) or 129/Sj (unique substrain of 129, Tolman et al., 2021) inbred mice. The *Lmx1b*^{V265D} mutation was discovered in an N-ethyl-N-nitrosourea (ENU) mutagenesis screen (Cross et al., 2014; Thaung et al., 2002; Tolman et al., 2021). These mice were then backcrossed to the C57BL/6J (Stock #000664) for at least 30 generations. All mice were treated in accordance with the Association for Research in Vision

and Ophthalmology's statement on the use of animals in ophthalmic research. The Institutional Animal Care and Use Committee of either Columbia University or Duke University approved all experimental protocols performed at their respective institutions.

NAM administration

Nicotinamide (NAM or niacinamide; Sigma-Aldrich, St. Louis, Missouri) was dissolved in the standard institutional drinking water to a dose of 550 mg/kg/day (low dose) based on the average volume mice consume. Untreated groups received the same drinking water without NAM. Water was changed once per week. Treatment was started at postnatal day 2. Births were checked daily between 9am-12pm to determine the pup's age.

Preparation of ocular cells

Columbia animals: Eyes were pooled from 4 animals to generate 1 sample (8 eyes total per pool). Two independent samples were processed. Mice were 2 months of age. Sex was balanced in each group.

Duke animals: One sample was generated from a pool of 4 animals (8 eyes total). All mice were male. Mice were 3 months of age.

Dissections: After euthanizing the animals, eyes were enucleated into fresh Dulbecco's Modified Eagle Medium (DMEM; Gibco) and subsequently dissected in DMEM. All dissection tools and surfaces were treated with RNAse zap (Ambion). For dissections, we removed the posterior eye by cutting between the limbus and sclera. The lens was then removed. Finally, we made a small circular cut in the anterior cornea, removing the middle 1/3rd of the area. Only limbal tissues were collected and all other tissues were removed. The remaining limbal tissue was minced and prepared for digestion.

Single Cell RNA Sequencing

Single-cell RNA sequencing (Columbia University): Tissues were digested enzymatically using Papain and Deoxyribonuclease I (Worthington Biochemical Corporation, Cat. no. LK003153) for 20 min at 37°C and stopped using Earl's balanced salt solution (EBSS, Thermo Fisher

Scientific, Cat no. 24010-043). Cells were triturated using an 18-gauge needle, centrifuged at 300g at 4 °C, washed with cold DMEM, and filtered using a 100 µm Flowmi Cell Strainer (H13680-0040, Bel-Art. Cells were resuspended in cold DMEM and placed on ice immediately. Cells were counted using Countess II automated cell counter and processed for 10x library preparation immediately (see below). All data will be deposited in the Gene Expression Omnibus (GEO) database and single cell portal.

Single-cell RNA sequencing (Duke University): Single cell dissociation was performed using Collagenase IV (Worthington Biochemical Cat. no. LS004188), Dispase II (Sigma Cat. No. D4693) and DNAse I (Roche Cat no. 50225500) for 60 min and then trypsin/EDTA for 10 min at 37°C. Cells were triturated using a 1 ml pipette tip, centrifuged at 300g at 4°C, washed with cold DMEM containing 10% FBS, and filtered using a 70 µm cell strainer (Fisher). Cells were resuspended in cold DMEM containing 5% FBS and placed on ice immediately and sent to Duke Genome Core Facility. Cells were counted using Countess II automated cell counter (the cell viability was 88%) and then immediately processed immediately (see below). All data will be deposited in the Gene Expression Omnibus (GEO) database and single cell portal.

Multiome (Columbia University): Limbal strip samples for multiome analysis were snap-frozen on dry ice immediately following dissection and stored at -80C until processing. To isolate nuclei, tissue was homogenized in 100 µL of chilled lysis buffer (10 mM Tris-HCl, pH 7.4, 10 mM NaCl, 3 mM MgCl2, 0.1% NP40, 0.1% Tween20, and 0.01% digitonin – from (Corces et al., 2017) supplemented with 1% BSA). Afterwards, samples were incubated for 5 min on ice, gently agitated by pipetting, and incubated for an additional 10 minutes on ice. We then added 1 mL of chilled wash buffer (10 mM Tris-HCl, pH 7.4, 10 mM NaCl, 3 mM MgCl2, 0.1% Tween 20, 1% BSA) to the cells and centrifuged at 500 rcf for 5 min at 4°C. Cells were resuspended in chilled Diluted Nuclei Buffer (PN-2000153, 10x Genomics) and filtered through a 40 µm Flowmi Cell Strainer (H13680-0040, Bel-Art). Cells were resuspended in cold DMEM and placed on ice immediately. An aliquot of nuclei suspension was stained with SYTOX green to count nuclei using Countess II automated cell counter and processed for 10x library preparation immediately (see below). All data will be deposited in the Gene Expression Omnibus (GEO) database and single cell portal.

Single-cell and single-nucleus RNA sequencing

Single-cell and single-nucleus RNA-seq was performed at the single-cell sequencing core in Columbia Genome Center (Columbia University) or Duke Molecular Genomics Core (MGC, Duke University). Single cells or nuclei were loaded into chromium microfluidic chips with v3 chemistry and barcoded with a 10x chromium controller (10x Genomics). RNA from the barcoded cells was reverse-transcribed, and sequencing libraries were constructed with a Chromium Single Cell v3 reagent kit (10x Genomics). Sequencing at both institutions was performed on NovaSeq 6000 (Illumina).

Sequencing data processing

Single cell and single nucleus sequencing: Raw reads were mapped to the mm10 reference genome by 10x Genomics Cell Ranger pipeline. “Seurat” (Version 4.0.1, Hao et al., 2021) was used to conduct all single-cell and single-nucleus sequencing analyses. Briefly, the dataset was filtered to contain cells with at least 200 expressed genes and genes with expression in more than three cells. Cells were also filtered for mitochondrial gene expression (<20% for single-cell and <5% for single-nucleus). The dataset was log-normalized and scaled. Biological incompatibility based on gene expression was used to identify doublets. For the scRNA-seq dataset generated at Columbia scRNA-seq, we performed unsupervised clustering followed by comparison to previous annotations (Balasubramanian et al., 2024; Patel et al., 2020; Thomson et al., 2021; van Zyl et al., 2020; van Zyl et al., 2022). A resolution parameter of 0.03 was used to match these data and previous annotations. Cluster 1 was then subclustered using unsupervised methods with a resolution parameter of 0.3. All cluster identities based on a combination of known marker genes and validation experiments. For additional datasets (Duke scRNA-seq, and Columbia snRNA-seq), parameters were manually adjusted cluster cells based on the Columbia scRNA-seq dataset. Marker genes were identified using Wilcoxon test implemented in Seurat using default parameters.

Multiome: Single-nucleus multiome data were quantified by 10x CellRanger and preprocessed according to integratedSeurat v4 (Hao et al., 2021) and Signac (Stuart et al., 2021). We filtered cells which have <500 and >80000 ATAC reads, have <500 and >25000 RNA reads, and have >10% mitochondrial reads. RNA-seq processing was performed using the same methods as scRNA-seq (above). ATAC-seq processing was performed using ArchR (version 1.0.2) (Granja et al., 2021), where we used default latent semantic indexing (LSI) approach to derive low-dimensional embedding followed by single-cell neighborhood construction and graph-based

clustering using the top 50 LSI dimensions excluding the first dimension. We assigned cell types using similar process based on marker peak accesibility and transferred cell type labels to the ATAC data.

***Lmx1b^{V265D}* analysis**: Data from limbal cells with the *Lmx1b^{V265D}* mutation (C57BL/6J background) were integrated with Wild-Type (WT) cells from the C57BL/6J strain only. Multiple approaches were used for normalizing data for integration in Seurat, including log normalization and SC transform. The relative number of cells in each cell cluster between WT and *V265D* mutant cells changed based on the integration technique. Therefore, we chose not to assess TM or other cell proportions between genotypes. Log normalization was selected for downstream analysis based on the log-transformed integrated WT clusters being more molecularly similar to the WT only clusters compared with the SC transform results.

Statistical data analysis

Hierarchical clustering: TM-containing cells were assessed by hierarchical clustering based on the similarity of the expression of the top 500 marker genes (ranked by P value) of each individual cluster. This analysis filtered out low-expressing genes (expressed in >10% of cells, with a logFC > 0.25 compared to other cells).

GO analysis: Gene ontology and pathway enrichment analysis were performed by comparing the differentially expressed genes in three scenarios:

1) All TM cells versus all other sequenced cells.
2) Each individual TM cell subtype against other TM cell subtypes.
3) WT versus *Lmx1b$^{V265D/+}$* TM cells.

For comparisons of all TM cells to all sequenced cells, pathway enrichment was compared against a background expression universe of genes expressed in any sequenced cell. For comparisons of individual TM cell subtypes, only genes expressed in trabecular meshwork cells were used as a background (P value cut-off 0.01, Timmons et al., 2015).

Gene set enrichment analysis (GSEA) was performed using the same set of differentially expressed genes from the above comparisons with the GseGO function. All pathways were assigned an enrichment score (< 0, underrepresented; > 0, enriched). Pathways that were

significantly enriched or underrepresented were also analyzed (P value cut-off 0.01). The R package ClusterProfiler was used for analysis (Yu et al., 2012).

Module score: From genome-wide association studies of IOP elevation (Blue Mountains Eye and Wellcome Trust Case Control, 2013; Choquet et al., 2017; Gao et al., 2018; Hysi et al., 2014; Khawaja et al., 2018; MacGregor et al., 2018; Nag et al., 2014; Ozel et al., 2014; Springelkamp et al., 2015; Springelkamp et al., 2017; van Koolwijk et al., 2012) or primary open-angle glaucoma (Bailey et al., 2016; Bonnemaijer et al., 2018; Choquet et al., 2018; Craig et al., 2020; Gharahkhani et al., 2021; Shiga et al., 2018; Verma et al., 2024), we curated a list of genes associated with the disease. Seurat's AddModuleScore function was applied to assess glaucoma disease risk for each cell type, using default parameters (24 bins for aggregation with 100 control features per analyzed feature).

Predicted ligand-receptor interactions: Predicted ligand-target links between interacting cells were identified using LRLoop (Xin et al., 2022), which was developed based on NicheNet (Browaeys et al., 2020). Briefly, the expression of genes in cell types is linked to a database of signaling and gene regulatory networks curated from prior information, enabling viable predictions of potential interactions between cell types. These interactions were calculated using target molecules from one cell type and ligands from multiple cell types. The top interactions, regardless of the cell type origin of the ligand, are represented in a Circos plot. Ligands were assigned to an individual TM cell subtype/subtypes based on the following criteria:

1) Exclusively assigned to a TM cell subtype if expressed > 1 transcript per ten thousand in a given cell type and expressed on average 4X more in that subtype compared to all other TM cell subtypes.
2) Assigned to multiple TM cell subtypes if expression is > 1 transcript per ten thousand in multiple cell types and average ligand expression is < 4X between those TM cell subtypes.
3) If ligand expression is low (< 1 transcript per ten thousand) across TM cell subtypes, the ligand is assigned to all subtypes that express the ligand.

Comparison to published datasets: To compare TM cell clusters across datasets, the top 10 marker genes (by P value) for TM cell subtypes in our dataset were compared to published marker genes in other TM cell datasets (Patel et al., 2020; Thomson et al., 2021; Ujiie et al.,

2023; van Zyl et al., 2020; van Zyl et al., 2022). Comparisons to both human and mouse TM cell data in the Van Zyl et al. dataset were performed using the Broad Institute single-cell browser: https://singlecell.broadinstitute.org/single_cell/study/SCP780.

ATAC: To refine ATAC-seq analysis, we applied ArchR (Granja et al., 2021) to remove any additional doublet cells and iteratively estimated LSI embedding using 500bp peaks tiled across the genome, followed by ArchR clustering and UMAP projection workflows to generate ATAC-seq cell clusters and two-dimensional embeddings (same cluster resolutions as above). Using marker gene expression, clusters were named and related to the single cell cluster identities. Using single-cell RNA-seq data collected earlier with annotated cell types, we projected single-cell ATAC-seq data onto the reference using ArchR's addGeneIntegrationMatrix function with default parameters. The integrated data with RNA-seq defined clusters were used for peak calling with MACS2, followed by marker peak identification (getMarkerFeatures) and TF enrichment (addMotifAnnotations) using the CisBP database (Weirauch et al., 2014). Finally, TF activity was quantified using chromVAR (Schep et al., 2017) and gene-peak links were inferred using the addPeak2GeneLinks function with default parameters. All significant TFs (VAR > 1) for each TM cell subtype were filtered by average RNA expression within the entire cluster using the Columbia University scRNA-seq data (better read depth than snRNA-seq). All significant TFs with no RNA expression were removed and all TFs with expression > 0.5 counts per 10,000 were prioritized for analysis. For a schematic of the analysis workflow, see *Figure 4A*. We then performed integrative analysis correlating the activity of each TF with its gene expression profile (both directly measured from multiome data and integrated expression data from reference scRNA-sequencing data). We used ArchR's correlateMatrices function, which reports Pearson correlation of normalized counts (TF activity matrix and gene expression / gene integration matrix) across 100 randomly subsampled neighborhoods of cells. We designated influential TFs as those with correlation > 0.5, adjusted p-value of correlation < 0.01, and chromVAR deviation above 75% of all TFs.

ATAC tracts: We chose marker genes (TM1: *Fn1*, TM2: *Gpc3*, TM3: *Acta2*) and plotted accessibility tracks. Motif footprinting analysis was performed using ArchR getFootprints function using CisBP-defined motif positions for RNA-defined cell types with default parameters.

Immunoflourescence and in situ hybridization

Sections with antibody staining: Enucleated adult eyes were fixed for 1 hour at 4°C in 4% paraformaldehyde (PFA, Electron Microscopy Science, Hatfield, PA) prepared in phosphate-buffered saline (1X PBS, 137 mM NaCl, 10 mM phosphate, 2.7 mM KCl, pH 7.4). Following fixation, a small window was made through the optic nerve head so that eyes would not shrivel during dehydration. Eyes were dehydrated in a 30% sucrose (Sigma-Aldrich, St. Louis, Missouri) in 1X PBS at 4°C until eyes sunk to the bottom of a 2 ml glass vial. Once sunken, eyes were embedded in optimal cutting temperature embedding medium (Fisher Scientific, Waltham, MA) and flash frozen on dry ice. Eyes were cryosectioned at 10 µm thickness in the sagittal plane. Sections were evenly spaced throughout the peripheral and central ocular regions.

Sections were washed three times with 1× PBS with 0.3% Triton X-100 for 5 min to quench residual fixation. The sections were then incubated with 10% Donkey serum (Sigma-Aldrich, St. Louis, Missouri) and 0.3% Triton X-100 in 1× PBS (blocking buffer) at room temperature for 1 h to block nonspecific binding of antibody and to permeabilize the tissue. The sections were then incubated with primary antibodies (see **Table S7**) in 200 µl blocking buffer overnight at 4°C. The sections were then washed three times for 5 m with 1× PBS with 0.3% Triton X-100. Primary antibodies were detected with the appropriate species-specific secondary antibody (all Alexa 488, 594, or 647 at 1:1000 dilution, Life Technologies, Grand Island, NY) diluted in 1× PBS with 0.3% Triton X-100 for 2 h at room temperature. The secondary detection solution also had DAPI at 1:1000 (Thermo Scientific, Waltham, MA) to label nuclei. The immunostained sections were washed three times for 5 m in 1× PBS with 0.3% Triton X-100. Sections were then cover-slipped using Flouromount (Sigma, St. Louis, MO).

Tyramide signal amplification (TSA): We performed a TSA reaction for a subtype of antibodies (See **Table S7**). TSA was performed on slides containing serial transverse cryosections of enucleated mouse eyes using the Akoya Biosciences TSA Plus Cyanine 3 detection kit (NEL744001KT). Freshly cut sections were allowed to come to room temperature and were then quenched for 10 minutes in a 1% hydrogen peroxide, 10% methanol in 0.01M phosphate buffered saline solution (1X PBS). The slides were rinsed in 1X PBS and allowed to block for 1 hour at room temperature in a blocking solution of 10% donkey serum, 0.3% Triton-X 100 in 1X PBS. Primaries for TSA were diluted 1:100 in blocking solution and approximately 200 microliters were added to the slides overnight at 4 degrees Celsius. The slides were then rinsed using a 0.3% Triton-X 100 in 1X PBS solution before being blocked in Tris-NaCl-blocking (TNB)

buffer for 1 hour at room temperature. Approximately 200 microliters of Horseradish peroxidase conjugated secondaries diluted 1:200 in TNB buffer were applied to the slides for 2 hours at room temperature. The slides were subsequently rinsed in Tris-NaCl-Tween (TNT) buffer. TSA Plus Working Solution was made by diluting the TSA Plus Stock Solution 1:50 in 1X Amplification Diluent. The TSA Plus Working Solution was added at a volume of 200 microliters for 7 minutes at room temperature. The slides were then washed in TNT buffer and approximately 200 microliters of non-amplified primaries for counterstaining diluted 1:200 in 10% donkey serum, 0.3% Triton-X 100 in 1X PBS blocking solution was applied overnight at 4 degrees Celsius. Secondary antibody detection and mounting were performed as above.

***in situ* hybridization**: We used the RNAscope® Multiplex Fluorescent Reagent Kit v2-Mm (Advanced Cell Diagnostics a Bio Techne Brand, Newark, CA). Probes for mouse *Lypd1* (#318361-C2), *Inmt* (#486371-C2), *Edn3* (#505841-C1), *Acta2* (α-SMA) (#319531-C3), and *Myoc* (#460981-C1) (also purchased from ACD Bio) were used. Fluorescent dyes Opal 690 (FP1497001KT) and Opal 620 (FP1495001KT) (Akoya Biosciences, Marlborough, MA) were used with each of these probes. Briefly, eyes from 3-month-old C57BL/6J were enucleated and fixed in 4% PFA for 24 h at 4°C. A window was made to the back of the eye cup, lens removed, and the anterior cup placed in 30% sucrose overnight at 4°C. Tissue was cryopreserved in OCT and placed at -80°C. Sections were cut at 12 μm thickness using SuperFrost Plus slides (Fisher Scientific, Hampton, NH).. RNAscope® was performed over two days as per manufacturer's protocol.

Whole mounts: Enucleated eyes were fixed for 2 hours at 4°C in 4% paraformaldehyde (PFA, Electron Microscopy Science, Hatfield, PA) prepared in phosphate-buffered saline (1× PBS, 137 mM NaCl, 10 mM phosphate, 2.7 mM KCl, pH 7.4). The postnatal eyes were dissected out following fixation. The anterior part of the eye was cut just posterior to the limbus (transition zone between cornea and sclera) as described in Kizhatil et al. Briefly, the iris, lens, ciliary body, and thin strip of retina were carefully removed to obtain the anterior eye cup. The anterior cup includes the cornea, limbus, and a small portion of retinal pigmented epithelium. Four centripetal cuts were made to relax the eye-cup and facilitate eventual mounting onto a slide after immunofluorescence.

Anterior eye cups were rinsed multiple times with 1× PBS. The eye cups were incubated with 3% bovine serum albumin and 1% Triton X-100 in 1× PBS (blocking buffer) at room temperature

for 1 h in 2 ml glass vials to block nonspecific binding of antibody and to permeabilize the tissue. The anterior cups were then incubated with primary antibodies (see **Table S7)** in 200 µl blocking buffer for 2 days, with rocking, at 4°C. The anterior cups were then washed three times over a 3-h period with 1× PBS. The primary antibodies were detected with the appropriate species-specific secondary antibody (all Alexa 488, 594, or 647 at 1:1,000 dilution, Life Technologies, Grand Island, NY) diluted in blocking buffer, which also had DAPI to label nuclei. The immunostained eye cups were washed three times over a 3-h period in 1× PBS. Eye cups were then whole-mounted on slides in Fluoromount (Sigma, St. Louis, MO).

Microscopy of drainage structures

Sections: Microscopy of sectioned postnatal eye slides was performed using an LSM SP8 confocal microscope (Leica) and 40×1.1 NA water immersion objective.

In situ: Images were taken using a Nikon Eclipse 90i confocal laser-scanning microscope (Melville). Z-stack images of 1 µm thickness, using the 40X objective lens, were taken of each section and converted into maximum projection images that were used for analysis.

Whole mounts: Microscopy was performed using an LSM SP8 confocal microscope (Leica) using a 63×1.4 NA glycerol immersion objective. The Mark and Find mode was used to automate collection of images, generating a folder full of Z stacks (Z = 0.3 µm) at various individual overlapping positions around the limbus. We examined n = 6 eyes total. We imaged a certain distance around the ocular circumference, with an equal representation from each ocular quadrant (1.5-2.5 mm total).

Postprocessing of whole-mount images

3D rendering: We followed the guidelines detailed in Kizhatil et al for visualizing SC and TM in 3D. Individual confocal Z stacks (.lsm files) were processed directly using Imaris 9.5 (Oxford Instruments, Carteret, NJ). The maximum intensity projection setting in Surpass mode of Imaris was used for 3D rendering. Controls and experimental image sets were treated identically. Images were oriented so that structures of interest were visible. For whole-mounted eyes, multiposition Z stacks generated using the Mark and Find setting on the confocal microscope were first imported into Imaris and converted into Imaris files (.ims files). The resulting Imaris

files were then stitched to generate a comprehensive Z stack encompassing the limbus using ImarisStitcher 9.5 (BitPlane AG, Zurich, Switzerland). The stitch was exported as an Imaris file and processed appropriately. For sections, images were taken in the Z-plane in focus. When making figures, the snapshot feature of Imaris was used to collect images at high resolution (1024×1024 pixels, 300 dpi).

TM marker location analysis

We defined the TM as the region between the inner wall of Schlemm's canal (SC, outer TM) and the anterior chamber (inner TM), extending from the anterior edge of the pars plana (posterior TM) to the posterior edge of Descemet's membrane of the corneal endothelium (anterior TM). The SC was defined using a panel of validated markers that varied to allow for different antibody species and different secondary antibodies to be used in conjunction with the SC markers (See Table S7 for list of antibodies, Kizhatil et al., 2014). Sections were only included in the scoring analysis if they met the following criteria:

1) Absence of obvious sectioning artifacts or abnormalities in the SC or TM region.
2) Distinguishability of all landmarks defining the TM.
3) Acceptably low background signal and absence of staining for non-specific or non-biological entities within the section.

For each section, the TM was segmented and analyzed in two separate ways. The anterior-posterior distance was measured, and the TM was divided in half along this axis at the midway point (**Figure S7C-D**). Using the surface feature in Imaris, the area of individual marker staining was measured, and the total area in both the anterior and posterior zones was calculated. Because markers are expressed at different levels, we normalized across markers by calculating the percent of individual marker expression in the anterior and posterior halves within each section. These percentage values in anterior and posterior halves were compared both within markers and across all markers of a given TM cell subtype by Student's t-test. The same analysis was repeated for the inner-outer halves by measuring the inner-outer TM distance at the midpoint of the TM (anterior-posterior axis) and dividing the TM in half at this value. A total of 130-160 sections were examined for markers of each individual TM cell subtype (see **Table S8** for breakdown across markers). These sections were from 10-12 individual eyes per cluster. All eyes were from WT mice of C57BL/6J background and between 3-6 months of age.

Additional analysis was performed by selecting a subset of examined sections with staining for select markers (TM1: MYOC antibody, TM2: CRYM antibody, *Inmt in situ*, TM3: α-SMA antibody). These sections were of exceptionally high quality and had: 1) Anterior-posterior TM length between 125-200 μm. 2) Inner-outer TM distance is between 15-30 μm.

With these selected sections, we subdivided the TM into eight different zones along both inner/outer and anterior/posterior axes (Figure S7F). For each individual section, we used Imaris to measure the anterior-posterior distance and divide the TM into three equal sectors (anterior, central, and posterior. Within each sector, the average depth of the TM was measured in Imaris. This calculation was used to divide the central and posterior sectors into three zones each (inner, intermediate, and outer). Because the anterior TM depth is thinner, we divided the anterior sector into two zones (inner and outer). In total, there were eight distinct zones.

The percent of total marker area was calculated for each of the eight zones for each individual section as described above. Percent of marker area in each zone was compared as shown in Figure 2 by one-way ANOVA followed by Tukey's honestly significant difference test.

Scleral cell marker analysis

For CD34 and LY6C1 expression, we examined greater than 60 sections from 4 eyes (CD34) and 3 eyes (LY6C1) respectively. The observed locations of these markers within the iridocorneal angle are described.

Whole mount marker location analysis

To analyze the expression of markers within the TM, we segmented the TM based on anatomy. Because various anatomical features including the pars plana were removed during the whole mount process, we used the SC (marked by PECAM) as the major anterior-posterior landmark. The TM was defined as the group of cells inner to the SC and not outside the anterior or posterior boundary of the SC.

Nuclear morphology

Anterior segment whole-mounts were used to examine nuclear morphology in 3D (TM1: MYOC, TM3: α-SMA, all antibodies). The TM was segmented as described above and the 'Surface' feature in Imaris used to demarcate TM cell nuclei. Nuclei that were analyzed were immediately adjacent to the immunolabeled TM marker and had to be well spaced from other nuclei. To ensure accuracy we used manual inspection to exclude: 1) Nuclei that were very close to other nuclei or groups of nuclei and 2) nuclei of cells that were labeled with a Schlemm's canal endothelial cell marker (PECAM) and/ or that projected into the lumen of SC. The 'Sphericity' tool was used to determine the degree of sphericity in Imaris. For each cell subtype, we assessed a total 60 nuclei from 6 eyes, assessing the first 10 randomly selected nuclei that met our inclusion criteria in each eye. Groups were compared by Student's t-test.

Availability of data and materials

All data generated or analyzed during this study are included in this published article (and its supplementary information files). Raw sequencing data is available on GEO and SCP.

Funding

This project was supported by National Eye Institute grant EY032507 (to S.W.M.J). Partial support was provided by EY11721, EY032062, and EY018606 (to SWMJ), Brightfocus grants CG2020004 (to S.W.M.J.), and G2021007 (to R.B.:), startup funds at Columbia University including the Precision Medicine Initiative, and the New York Fund for Innovation in Research and Scientific Talent (NYFIRST; EMPIRE CU19-2660). At Duke, the work was also supported by NEI grants EY028608, EY022359 (to WDS). Supported also came from Vision Core grants P30EY019007 (Columbia University), P30EY005722 (Duke University) and an unrestricted departmental award from Research to Prevent Blindness (Columbia University and Duke University). The content is solely the responsibility of the authors and does not necessarily represent the official views of the National Institutes of Health. SWMJ is the Robert Burch III Professor of Ophthalmic Sciences.

Authors' contributions

NT – conceived and designed and performed experiments, analyzed data, wrote the manuscript

RB – conceived and designed and performed experiments, analyzed data, edited manuscript

TL – conceived and designed analyses, analyzed data, edited manuscript

VBC –designed analyses, performed experiments

RK –designed analyses, performed experiments

GL –designed analyses, performed experiments

SM – performed experiments

MS – assisted data anal edited manuscript

CM – edited manuscript assisted w lab management and mouse colonies /physiology

DS – conceived and designed experiments, analyzed data, edited manuscript, sought and obtained funding

JQ – conceived and designed analyses, edited manuscript

SJ – conceived and oversaw overall study and designed experiments, analyzed data, wrote and edited manuscript, sought and obtained funding

Acknowledgments

The authors would like to thank the members the Simon John Laboratory for experimental and technical assistance, Drs. Krish Kizhatil and Chi Zhang for reading and editing the manuscript, the Institute of Comparative Medicine and Devanshi Ragha at Columbia University for animal and veterinary care, the JP Sulzberger Columbia Genome Center and Duke University Molecular Genomics Core for assistance with genomics studies, and the P30EY019007 Columbia Shared Resources grant for histological experiments. Dr. Simon John is the Robert L. Burch III Professor of Ophthalmic Sciences at Columbia University's Vagelos College of Physicians and Surgeons.

References

Aboobakar, I. F., Kinzy, T. G., Zhao, Y., Fan, B., Pasquale, L. R., Qassim, A., Kolovos, A., Schmidt, J. M., Craig, J. E., Cooke Bailey, J. N. et al. (2023). Mitochondrial TXNRD2 and ME3 Genetic Risk Scores Are Associated with Specific Primary Open-Angle Glaucoma Phenotypes. *Ophthalmology* **130**, 756-763.

Abu-Amero, K. K., Morales, J. and Bosley, T. M. (2006). Mitochondrial abnormalities in patients with primary open-angle glaucoma. *Invest Ophthalmol Vis Sci* **47**, 2533-41.

Abu-Hassan, D. W., Acott, T. S. and Kelley, M. J. (2014). The Trabecular Meshwork: A Basic Review of Form and Function. *J Ocul Biol* **2**.

Acott, T. S. and Kelley, M. J. (2008). Extracellular matrix in the trabecular meshwork. *Exp Eye Res* **86**, 543-61.

Acott, T. S., Kingsley, P. D., Samples, J. R. and Van Buskirk, E. M. (1988). Human trabecular meshwork organ culture: morphology and glycosaminoglycan synthesis. *Invest Ophthalmol Vis Sci* **29**, 90-100.

Akula, M., Taiyab, A., Deschamps, P., Yee, S., Ball, A. K., Williams, T. and West-Mays, J. A. (2020). AP-2beta is required for formation of the murine trabecular meshwork and Schlemm's canal. *Exp Eye Res* **195**, 108042.

Ali, M., McKibbin, M., Booth, A., Parry, D. A., Jain, P., Riazuddin, S. A., Hejtmancik, J. F., Khan, S. N., Firasat, S., Shires, M. et al. (2009). Null mutations in LTBP2 cause primary congenital glaucoma. *Am J Hum Genet* **84**, 664-71.

Aspelund, A., Tammela, T., Antila, S., Nurmi, H., Leppanen, V. M., Zarkada, G., Stanczuk, L., Francois, M., Makinen, T., Saharinen, P. et al. (2014). The Schlemm's canal is a VEGF-C/VEGFR-3-responsive lymphatic-like vessel. *J Clin Invest* **124**, 3975-86.

Aumailley, M. (2013). The laminin family. *Cell Adh Migr* **7**, 48-55.

Bailey, J. N., Loomis, S. J., Kang, J. H., Allingham, R. R., Gharahkhani, P., Khor, C. C., Burdon, K. P., Aschard, H., Chasman, D. I., Igo, R. P., Jr. et al. (2016). Genome-wide association analysis identifies TXNRD2, ATXN2 and FOXC1 as susceptibility loci for primary open-angle glaucoma. *Nat Genet* **48**, 189-94.

Balasubramanian, R., Kizhatil, K., Li, T., Tolman, N., Bhandari, A., Clark, G., Bupp-Chickering, V., Kelly, R. A., Zhou, S., Peregrin, J. et al. (2024). Transcriptomic profiling of Schlemm's canal cells reveals a lymphatic-biased identity and three major cell states. *bioRxiv*.

Bergman, O., Hakansson, A., Westberg, L., Belin, A. C., Sydow, O., Olson, L., Holmberg, B., Fratiglioni, L., Backman, L., Eriksson, E. et al. (2009). Do polymorphisms in transcription factors LMX1A and LMX1B influence the risk for Parkinson's disease? *J Neural Transm (Vienna)* **116**, 333-8.

Biernacka, A., Dobaczewski, M. and Frangogiannis, N. G. (2011). TGF-beta signaling in fibrosis. *Growth Factors* **29**, 196-202.

Blue Mountains Eye, S. and Wellcome Trust Case Control, C. (2013). Genome-wide association study of intraocular pressure identifies the GLCCI1/ICA1 region as a glaucoma susceptibility locus. *Hum Mol Genet* **22**, 4653-60.

Bonnemaijer, P. W. M., Iglesias, A. I., Nadkarni, G. N., Sanyiwa, A. J., Hassan, H. G., Cook, C., Group, G. S., Simcoe, M., Taylor, K. D., Schurmann, C. et al. (2018). Genome-wide association study of primary open-angle glaucoma in continental and admixed African populations. *Hum Genet* **137**, 847-862.

Browaeys, R., Saelens, W. and Saeys, Y. (2020). NicheNet: modeling intercellular communication by linking ligands to target genes. *Nat Methods* **17**, 159-162.

Buffault, J., Labbe, A., Hamard, P., Brignole-Baudouin, F. and Baudouin, C. (2020). The trabecular meshwork: Structure, function and clinical implications. A review of the literature. *J Fr Ophtalmol* **43**, e217-e230.

Chen, H., Lun, Y., Ovchinnikov, D., Kokubo, H., Oberg, K. C., Pepicelli, C. V., Gan, L., Lee, B. and Johnson, R. L. (1998). Limb and kidney defects in Lmx1b mutant mice suggest an involvement of LMX1B in human nail patella syndrome. *Nat Genet* **19**, 51-5.

Chen, L., Zhao, Y. and Zhang, H. (2016). Comparative Anatomy of the Trabecular Meshwork, the Optic Nerve Head and the Inner Retina in Rodent and Primate Models Used for Glaucoma Research. *Vision (Basel)* **1**.

Choquet, H., Paylakhi, S., Kneeland, S. C., Thai, K. K., Hoffmann, T. J., Yin, J., Kvale, M. N., Banda, Y., Tolman, N. G., Williams, P. A. et al. (2018). A multiethnic genome-wide association study of primary open-angle glaucoma identifies novel risk loci. *Nat Commun* **9**, 2278.

Choquet, H., Thai, K. K., Yin, J., Hoffmann, T. J., Kvale, M. N., Banda, Y., Schaefer, C., Risch, N., Nair, K. S., Melles, R. et al. (2017). A large multi-ethnic genome-wide association study identifies novel genetic loci for intraocular pressure. *Nat Commun* **8**, 2108.

Comes, N. and Borras, T. (2009). Individual molecular response to elevated intraocular pressure in perfused postmortem human eyes. *Physiol Genomics* **38**, 205-25.

Corces, M. R., Trevino, A. E., Hamilton, E. G., Greenside, P. G., Sinnott-Armstrong, N. A., Vesuna, S., Satpathy, A. T., Rubin, A. J., Montine, K. S., Wu, B. et al. (2017). An improved ATAC-seq protocol reduces background and enables interrogation of frozen tissues. *Nat Methods* **14**, 959-962.

Craig, J. E., Han, X., Qassim, A., Hassall, M., Cooke Bailey, J. N., Kinzy, T. G., Khawaja, A. P., An, J., Marshall, H., Gharahkhani, P. et al. (2020). Multitrait analysis of glaucoma identifies new risk loci and enables polygenic prediction of disease susceptibility and progression. *Nat Genet* **52**, 160-166.

Cross, S. H., Macalinao, D. G., McKie, L., Rose, L., Kearney, A. L., Rainger, J., Thaung, C., Keighren, M., Jadeja, S., West, K. et al. (2014). A dominant-negative mutation of mouse Lmx1b causes glaucoma and is semi-lethal via LDB1-mediated dimerization [corrected]. *PLoS Genet* **10**, e1004359.

de Kater, A. W., Shahsafaei, A. and Epstein, D. L. (1992). Localization of smooth muscle and nonmuscle actin isoforms in the human aqueous outflow pathway. *Invest Ophthalmol Vis Sci* **33**, 424-9.

De Moraes, C. G., John, S. W. M., Williams, P. A., Blumberg, D. M., Cioffi, G. A. and Liebmann, J. M. (2022). Nicotinamide and Pyruvate for Neuroenhancement in Open-Angle Glaucoma: A Phase 2 Randomized Clinical Trial. *JAMA Ophthalmol* **140**, 11-18.

Desronvil, T., Logan-Wyatt, D., Abdrabou, W., Triana, M., Jones, R., Taheri, S., Del Bono, E., Pasquale, L. R., Olivier, M., Haines, J. L. et al. (2010). Distribution of COL8A2 and COL8A1 gene variants in Caucasian primary open angle glaucoma patients with thin central corneal thickness. *Mol Vis* **16**, 2185-91.

DeWane, G., Salvi, A. M. and DeMali, K. A. (2021). Fueling the cytoskeleton - links between cell metabolism and actin remodeling. *J Cell Sci* **134**.

Doucet-Beaupre, H., Gilbert, C., Profes, M. S., Chabrat, A., Pacelli, C., Giguere, N., Rioux, V., Charest, J., Deng, Q., Laguna, A. et al. (2016). Lmx1a and Lmx1b regulate mitochondrial functions and survival of adult midbrain dopaminergic neurons. *Proc Natl Acad Sci U S A* **113**, E4387-96.

Ethier, C. R. (2002). The inner wall of Schlemm's canal. *Exp Eye Res* **74**, 161-72.

Frangogiannis, N. (2020). Transforming growth factor-beta in tissue fibrosis. *J Exp Med* **217**, e20190103.

Fuchshofer, R. and Tamm, E. R. (2009). Modulation of extracellular matrix turnover in the trabecular meshwork. *Exp Eye Res* **88**, 683-8.

Fuchshofer, R., Welge-Lussen, U., Lutjen-Drecoll, E. and Birke, M. (2006). Biochemical and morphological analysis of basement membrane component expression in corneoscleral and cribriform human trabecular meshwork cells. *Invest Ophthalmol Vis Sci* **47**, 794-801.

Fujimoto, T., Inoue, T., Maki, K., Inoue-Mochita, M. and Tanihara, H. (2016). Vascular Endothelial Growth Factor-A Increases the Aqueous Humor Outflow Facility. *PLoS One* **11**, e0161332.

Gao, X. R., Huang, H., Nannini, D. R., Fan, F. and Kim, H. (2018). Genome-wide association analyses identify new loci influencing intraocular pressure. *Hum Mol Genet* **27**, 2205-2213.

Genovesi, S., Giussani, M., Orlando, A., Lieti, G., Viazzi, F. and Parati, G. (2022). Relationship between endothelin and nitric oxide pathways in the onset and maintenance of hypertension in children and adolescents. *Pediatr Nephrol* **37**, 537-545.

Gharahkhani, P., Jorgenson, E., Hysi, P., Khawaja, A. P., Pendergrass, S., Han, X., Ong, J. S., Hewitt, A. W., Segre, A. V., Rouhana, J. M. et al. (2021). Genome-wide meta-analysis identifies 127 open-angle glaucoma loci with consistent effect across ancestries. *Nat Commun* **12**, 1258.

Gomes, A. P., Price, N. L., Ling, A. J., Moslehi, J. J., Montgomery, M. K., Rajman, L., White, J. P., Teodoro, J. S., Wrann, C. D., Hubbard, B. P. et al. (2013). Declining NAD(+) induces a pseudohypoxic state disrupting nuclear-mitochondrial communication during aging. *Cell* **155**, 1624-38.

Granja, J. M., Corces, M. R., Pierce, S. E., Bagdatli, S. T., Choudhry, H., Chang, H. Y. and Greenleaf, W. J. (2021). ArchR is a scalable software package for integrative single-cell chromatin accessibility analysis. *Nat Genet* **53**, 403-411.

Hao, Y., Hao, S., Andersen-Nissen, E., Mauck, W. M., 3rd, Zheng, S., Butler, A., Lee, M. J., Wilk, A. J., Darby, C., Zager, M. et al. (2021). Integrated analysis of multimodal single-cell data. *Cell* **184**, 3573-3587 e29.

Herrmann, H., Bar, H., Kreplak, L., Strelkov, S. V. and Aebi, U. (2007). Intermediate filaments: from cell architecture to nanomechanics. *Nat Rev Mol Cell Biol* **8**, 562-73.

Hui, F., Tang, J., Williams, P. A., McGuinness, M. B., Hadoux, X., Casson, R. J., Coote, M., Trounce, I. A., Martin, K. R., van Wijngaarden, P. et al. (2020). Improvement in inner retinal function in glaucoma with nicotinamide (vitamin B3) supplementation: A crossover randomized clinical trial. *Clin Exp Ophthalmol* **48**, 903-914.

Hysi, P. G., Cheng, C. Y., Springelkamp, H., Macgregor, S., Bailey, J. N. C., Wojciechowski, R., Vitart, V., Nag, A., Hewitt, A. W., Hohn, R. et al. (2014). Genome-wide analysis of multi-ancestry cohorts identifies new loci influencing intraocular pressure and susceptibility to glaucoma. *Nat Genet* **46**, 1126-1130.

Imai, S. and Guarente, L. (2014). NAD+ and sirtuins in aging and disease. *Trends Cell Biol* **24**, 464-71.

Jang, S. Y., Kang, H. T. and Hwang, E. S. (2012). Nicotinamide-induced mitophagy: event mediated by high NAD+/NADH ratio and SIRT1 protein activation. *J Biol Chem* **287**, 19304-14.

Jimenez-Moreno, N., Kollareddy, M., Stathakos, P., Moss, J. J., Anton, Z., Shoemark, D. K., Sessions, R. B., Witzgall, R., Caldwell, M. and Lane, J. D. (2023). ATG8-dependent LMX1B-autophagy crosstalk shapes human midbrain dopaminergic neuronal resilience. *J Cell Biol* **222**.

Johnson, M. (2006). 'What controls aqueous humour outflow resistance?'. *Exp Eye Res* **82**, 545-57.

Kabra, M., Zhang, W., Rathi, S., Mandal, A. K., Senthil, S., Pyatla, G., Ramappa, M., Banerjee, S., Shekhar, K., Marmamula, S. et al. (2017). Angiopoietin receptor TEK interacts with CYP1B1 in primary congenital glaucoma. *Hum Genet* **136**, 941-949.

Kang, H. T. and Hwang, E. S. (2009). Nicotinamide enhances mitochondria quality through autophagy activation in human cells. *Aging Cell* **8**, 426-38.

Keller, K. E. and Acott, T. S. (2013). The Juxtacanalicular Region of Ocular Trabecular Meshwork: A Tissue with a Unique Extracellular Matrix and Specialized Function. *J Ocul Biol* **1**, 3.

Keller, K. E., Aga, M., Bradley, J. M., Kelley, M. J. and Acott, T. S. (2009). Extracellular matrix turnover and outflow resistance. *Exp Eye Res* **88**, 676-82.

Keller, K. E. and Peters, D. M. (2022). Pathogenesis of glaucoma: Extracellular matrix dysfunction in the trabecular meshwork-A review. *Clin Exp Ophthalmol* **50**, 163-182.

Khawaja, A. P., Cooke Bailey, J. N., Kang, J. H., Allingham, R. R., Hauser, M. A., Brilliant, M., Budenz, D. L., Christen, W. G., Fingert, J., Gaasterland, D. et al. (2016). Assessing the Association of Mitochondrial Genetic Variation With Primary Open-Angle Glaucoma Using Gene-Set Analyses. *Invest Ophthalmol Vis Sci* **57**, 5046-5052.

Khawaja, A. P., Cooke Bailey, J. N., Wareham, N. J., Scott, R. A., Simcoe, M., Igo, R. P., Jr., Song, Y. E., Wojciechowski, R., Cheng, C. Y., Khaw, P. T. et al. (2018). Genome-wide analyses identify 68 new loci associated with intraocular pressure and improve risk prediction for primary open-angle glaucoma. *Nat Genet* **50**, 778-782.

Kizhatil, K., Ryan, M., Marchant, J. K., Henrich, S. and John, S. W. (2014). Schlemm's canal is a unique vessel with a combination of blood vascular and lymphatic phenotypes that forms by a novel developmental process. *PLoS Biol* **12**, e1001912.

Knepper, P. A., Farbman, A. I. and Telser, A. G. (1981). Aqueous outflow pathway glycosaminoglycans. *Exp Eye Res* **32**, 265-77.

Knepper, P. A., Goossens, W., Hvizd, M. and Palmberg, P. F. (1996). Glycosaminoglycans of the human trabecular meshwork in primary open-angle glaucoma. *Invest Ophthalmol Vis Sci* **37**, 1360-7.

Knepper, P. A. and McLone, D. G. (1985). Glycosaminoglycans and outflow pathways of the eye and brain. *Pediatr Neurosci* **12**, 240-51.

Libby, R. T., Smith, R. S., Savinova, O. V., Zabaleta, A., Martin, J. E., Gonzalez, F. J. and John, S. W. (2003). Modification of ocular defects in mouse developmental glaucoma models by tyrosinase. *Science* **299**, 1578-81.

Liu, C. Y., Birk, D. E., Hassell, J. R., Kane, B. and Kao, W. W. (2003). Keratocan-deficient mice display alterations in corneal structure. *J Biol Chem* **278**, 21672-7.

Lo Faro, V., Nolte, I. M., Ten Brink, J. B., Snieder, H., Jansonius, N. M. and Bergen, A. A. (2021). Mitochondrial Genome Study Identifies Association Between Primary

Open-Angle Glaucoma and Variants in MT-CYB, MT-ND4 Genes and Haplogroups. *Front Genet* **12**, 781189.

Lopez, I. A., Rosenblatt, M. I., Kim, C., Galbraith, G. C., Jones, S. M., Kao, L., Newman, D., Liu, W., Yeh, S., Pushkin, A. et al. (2009). Slc4a11 gene disruption in mice: cellular targets of sensorineuronal abnormalities. *J Biol Chem* **284**, 26882-96.

MacGregor, S., Ong, J. S., An, J., Han, X., Zhou, T., Siggs, O. M., Law, M. H., Souzeau, E., Sharma, S., Lynn, D. J. et al. (2018). Genome-wide association study of intraocular pressure uncovers new pathways to glaucoma. *Nat Genet* **50**, 1067-1071.

Meng, X. M., Nikolic-Paterson, D. J. and Lan, H. Y. (2016). TGF-beta: the master regulator of fibrosis. *Nat Rev Nephrol* **12**, 325-38.

Monje, P. V., Sant, D. and Wang, G. (2018). Phenotypic and Functional Characteristics of Human Schwann Cells as Revealed by Cell-Based Assays and RNA-SEQ. *Mol Neurobiol* **55**, 6637-6660.

Mouchiroud, L., Houtkooper, R. H., Moullan, N., Katsyuba, E., Ryu, D., Canto, C., Mottis, A., Jo, Y. S., Viswanathan, M., Schoonjans, K. et al. (2013). The NAD(+)/Sirtuin Pathway Modulates Longevity through Activation of Mitochondrial UPR and FOXO Signaling. *Cell* **154**, 430-41.

Munger, J. S. and Sheppard, D. (2011). Cross talk among TGF-beta signaling pathways, integrins, and the extracellular matrix. *Cold Spring Harb Perspect Biol* **3**, a005017.

Nag, A., Venturini, C., Small, K. S., International Glaucoma Genetics, C., Young, T. L., Viswanathan, A. C., Mackey, D. A., Hysi, P. G. and Hammond, C. (2014). A genome-wide association study of intra-ocular pressure suggests a novel association in the gene FAM125B in the TwinsUK cohort. *Hum Mol Genet* **23**, 3343-8.

Nitzan, E., Pfaltzgraff, E. R., Labosky, P. A. and Kalcheim, C. (2013). Neural crest and Schwann cell progenitor-derived melanocytes are two spatially segregated populations similarly regulated by Foxd3. *Proc Natl Acad Sci U S A* **110**, 12709-14.

Ostojic, J., Grozdanic, S., Syed, N. A., Hargrove, M. S., Trent, J. T., 3rd, Kuehn, M. H., Kardon, R. H., Kwon, Y. H. and Sakaguchi, D. S. (2008). Neuroglobin and cytoglobin distribution in the anterior eye segment: a comparative immunohistochemical study. *J Histochem Cytochem* **56**, 863-72.

Overby, D. R., Bertrand, J., Schicht, M., Paulsen, F., Stamer, W. D. and Lutjen-Drecoll, E. (2014). The structure of the trabecular meshwork, its connections to the ciliary muscle, and the effect of pilocarpine on outflow facility in mice. *Invest Ophthalmol Vis Sci* **55**, 3727-36.

Overby, D. R., Stamer, W. D. and Johnson, M. (2009). The changing paradigm of outflow resistance generation: towards synergistic models of the JCT and inner wall endothelium. *Exp Eye Res* **88**, 656-70.

Ozel, A. B., Moroi, S. E., Reed, D. M., Nika, M., Schmidt, C. M., Akbari, S., Scott, K., Rozsa, F., Pawar, H., Musch, D. C. et al. (2014). Genome-wide association study and meta-analysis of intraocular pressure. *Hum Genet* **133**, 41-57.

Patel, G., Fury, W., Yang, H., Gomez-Caraballo, M., Bai, Y., Yang, T., Adler, C., Wei, Y., Ni, M., Schmitt, H. et al. (2020). Molecular taxonomy of human ocular outflow tissues defined by single-cell transcriptomics. *Proc Natl Acad Sci U S A* **117**, 12856-12867.

Patel, S. P. and Parker, M. D. (2015). SLC4A11 and the Pathophysiology of Congenital Hereditary Endothelial Dystrophy. *Biomed Res Int* **2015**, 475392.

Petriti, B., Rabiolo, A., Chau, K. Y., Williams, P. A., Montesano, G., Lascaratos, G. and Garway-Heath, D. F. (2024). Peripheral blood mononuclear cell respiratory function is associated with progressive glaucomatous vision loss. *Nat Med* **30**, 2362-2370.

Quigley, H. A. and Broman, A. T. (2006). The number of people with glaucoma worldwide in 2010 and 2020. *Br J Ophthalmol* **90**, 262-7.

Rao, P. V., Deng, P., Sasaki, Y. and Epstein, D. L. (2005). Regulation of myosin light chain phosphorylation in the trabecular meshwork: role in aqueous humour outflow facility. *Exp Eye Res* **80**, 197-206.

Rao, P. V., Deng, P. F., Kumar, J. and Epstein, D. L. (2001). Modulation of aqueous humor outflow facility by the Rho kinase-specific inhibitor Y-27632. *Invest Ophthalmol Vis Sci* **42**, 1029-37.

Reina-Torres, E., Boussommier-Calleja, A., Sherwood, J. M. and Overby, D. R. (2020). Aqueous Humor Outflow Requires Active Cellular Metabolism in Mice. *Invest Ophthalmol Vis Sci* **61**, 45.

Reina-Torres, E., Wen, J. C., Liu, K. C., Li, G., Sherwood, J. M., Chang, J. Y., Challa, P., Flugel-Koch, C. M., Stamer, W. D., Allingham, R. R. et al. (2017). VEGF as a Paracrine Regulator of Conventional Outflow Facility. *Invest Ophthalmol Vis Sci* **58**, 1899-1908.

Roberts, A. L., Mavlyutov, T. A., Perlmutter, T. E., Curry, S. M., Harris, S. L., Chauhan, A. K. and McDowell, C. M. (2020). Fibronectin extra domain A (FN-EDA) elevates intraocular pressure through Toll-like receptor 4 signaling. *Sci Rep* **10**, 9815.

Saharinen, P., Eklund, L. and Alitalo, K. (2017). Therapeutic targeting of the angiopoietin-TIE pathway. *Nat Rev Drug Discov* **16**, 635-661.

Schep, A. N., Wu, B., Buenrostro, J. D. and Greenleaf, W. J. (2017). chromVAR: inferring transcription-factor-associated accessibility from single-cell epigenomic data. *Nat Methods* **14**, 975-978.

Schondorf, D. C., Ivanyuk, D., Baden, P., Sanchez-Martinez, A., De Cicco, S., Yu, C., Giunta, I., Schwarz, L. K., Di Napoli, G., Panagiotakopoulou, V. et al. (2018). The NAD+ Precursor Nicotinamide Riboside Rescues Mitochondrial Defects and Neuronal Loss in iPSC and Fly Models of Parkinson's Disease. *Cell Rep* **23**, 2976-2988.

Shibuya, M. (2011). Vascular Endothelial Growth Factor (VEGF) and Its Receptor (VEGFR) Signaling in Angiogenesis: A Crucial Target for Anti- and Pro-Angiogenic Therapies. *Genes Cancer* **2**, 1097-105.

Shifera, A. S., Trivedi, S., Chau, P., Bonnemaison, L. H., Iguchi, R. and Alvarado, J. A. (2010). Constitutive secretion of chemokines by cultured human trabecular meshwork cells. *Exp Eye Res* **91**, 42-7.

Shiga, Y., Akiyama, M., Nishiguchi, K. M., Sato, K., Shimozawa, N., Takahashi, A., Momozawa, Y., Hirata, M., Matsuda, K., Yamaji, T. et al. (2018). Genome-wide association study identifies seven novel susceptibility loci for primary open-angle glaucoma. *Hum Mol Genet* **27**, 1486-1496.

Smith, R. S., Zabaleta, A., Savinova, O. V. and John, S. W. (2001). The mouse anterior chamber angle and trabecular meshwork develop without cell death. *BMC Dev Biol* **1**, 3.

Song, S. B., Park, J. S., Jang, S. Y. and Hwang, E. S. (2021). Nicotinamide Treatment Facilitates Mitochondrial Fission through Drp1 Activation Mediated by SIRT1-Induced Changes in Cellular Levels of cAMP and Ca(2). *Cells* **10**.

Souma, T., Tompson, S. W., Thomson, B. R., Siggs, O. M., Kizhatil, K., Yamaguchi, S., Feng, L., Limviphuvadh, V., Whisenhunt, K. N., Maurer-Stroh, S. et al. (2016).

Angiopoietin receptor TEK mutations underlie primary congenital glaucoma with variable expressivity. *J Clin Invest* **126**, 2575-87.

Springelkamp, H., Iglesias, A. I., Cuellar-Partida, G., Amin, N., Burdon, K. P., van Leeuwen, E. M., Gharahkhani, P., Mishra, A., van der Lee, S. J., Hewitt, A. W. et al. (2015). ARHGEF12 influences the risk of glaucoma by increasing intraocular pressure. *Hum Mol Genet* **24**, 2689-99.

Springelkamp, H., Iglesias, A. I., Mishra, A., Hohn, R., Wojciechowski, R., Khawaja, A. P., Nag, A., Wang, Y. X., Wang, J. J., Cuellar-Partida, G. et al. (2017). New insights into the genetics of primary open-angle glaucoma based on meta-analyses of intraocular pressure and optic disc characteristics. *Hum Mol Genet* **26**, 438-453.

Stamer, W. D. and Acott, T. S. (2012). Current understanding of conventional outflow dysfunction in glaucoma. *Curr Opin Ophthalmol* **23**, 135-43.

Stamer, W. D. and Clark, A. F. (2017). The many faces of the trabecular meshwork cell. *Exp Eye Res* **158**, 112-123.

Stratton, J. A., Kumar, R., Sinha, S., Shah, P., Stykel, M., Shapira, Y., Midha, R. and Biernaskie, J. (2017). Purification and Characterization of Schwann Cells from Adult Human Skin and Nerve. *eNeuro* **4**.

Stuart, T., Srivastava, A., Madad, S., Lareau, C. A. and Satija, R. (2021). Single-cell chromatin state analysis with Signac. *Nat Methods* **18**, 1333-1341.

Sweeney, E., Fryer, A., Mountford, R., Green, A. and McIntosh, I. (2003). Nail patella syndrome: a review of the phenotype aided by developmental biology. *J Med Genet* **40**, 153-62.

Syriani, E., Cuesto, G., Abad, E., Pelaez, T., Gual, A., Pintor, J., Morales, M. and Gasull, X. (2009). Effects of platelet-derived growth factor on aqueous humor dynamics. *Invest Ophthalmol Vis Sci* **50**, 3833-9.

Tamm, E. R. (2009). The trabecular meshwork outflow pathways: structural and functional aspects. *Exp Eye Res* **88**, 648-55.

Thaung, C., West, K., Clark, B. J., McKie, L., Morgan, J. E., Arnold, K., Nolan, P. M., Peters, J., Hunter, A. J., Brown, S. D. et al. (2002). Novel ENU-induced eye mutations in the mouse: models for human eye disease. *Hum Mol Genet* **11**, 755-67.

Thieme, H., Nuskovski, M., Nass, J. U., Pleyer, U., Strauss, O. and Wiederholt, M. (2000). Mediation of calcium-independent contraction in trabecular meshwork through protein kinase C and rho-A. *Invest Ophthalmol Vis Sci* **41**, 4240-6.

Thomson, B. R., Grannonico, M., Liu, F., Liu, M., Mendapara, P., Xu, Y., Liu, X. and Quaggin, S. E. (2020). Angiopoietin-1 Knockout Mice as a Genetic Model of Open-Angle Glaucoma. *Transl Vis Sci Technol* **9**, 16.

Thomson, B. R., Liu, P., Onay, T., Du, J., Tompson, S. W., Misener, S., Purohit, R. R., Young, T. L., Jin, J. and Quaggin, S. E. (2021). Cellular crosstalk regulates the aqueous humor outflow pathway and provides new targets for glaucoma therapies. *Nat Commun* **12**, 6072.

Tian, B., Gabelt, B. T., Geiger, B. and Kaufman, P. L. (2009). The role of the actomyosin system in regulating trabecular fluid outflow. *Exp Eye Res* **88**, 713-7.

Tian, B. and Kaufman, P. L. (2005). Effects of the Rho kinase inhibitor Y-27632 and the phosphatase inhibitor calyculin A on outflow facility in monkeys. *Exp Eye Res* **80**, 215-25.

Timmons, J. A., Szkop, K. J. and Gallagher, I. J. (2015). Multiple sources of bias confound functional enrichment analysis of global -omics data. *Genome Biol* **16**, 186.

Tolman, N. G., Balasubramanian, R., Macalinao, D. G., Kearney, A. L., MacNicoll, K. H., Montgomery, C. L., de Vries, W. N., Jackson, I. J., Cross, S. H., Kizhatil, K. et al. (2021). Genetic background modifies vulnerability to glaucoma-related phenotypes in Lmx1b mutant mice. *Dis Model Mech* **14**.

Toyono, T., Usui, T., Yokoo, S., Taketani, Y., Nakagawa, S., Kuroda, M., Yamagami, S. and Amano, S. (2015). Angiopoietin-like 7 is an anti-angiogenic protein required to prevent vascularization of the cornea. *PLoS One* **10**, e0116838.

Ujiie, N., Norden, P. R., Fang, R., Beckmann, L., Cai, Z., Kweon, J., Liu, T., Tan, C., Kuhn, M. S., Stamer, W. D. et al. (2023). Differential roles of FOXC2 in the trabecular meshwork and Schlemm's canal in glaucomatous pathology. *Life Sci Alliance* **6**.

van Koolwijk, L. M., Ramdas, W. D., Ikram, M. K., Jansonius, N. M., Pasutto, F., Hysi, P. G., Macgregor, S., Janssen, S. F., Hewitt, A. W., Viswanathan, A. C. et al. (2012). Common genetic determinants of intraocular pressure and primary open-angle glaucoma. *PLoS Genet* **8**, e1002611.

van Zyl, T., Yan, W., McAdams, A., Peng, Y. R., Shekhar, K., Regev, A., Juric, D. and Sanes, J. R. (2020). Cell atlas of aqueous humor outflow pathways in eyes of humans and four model species provides insight into glaucoma pathogenesis. *Proc Natl Acad Sci U S A* **117**, 10339-10349.

van Zyl, T., Yan, W., McAdams, A. M., Monavarfeshani, A., Hageman, G. S. and Sanes, J. R. (2022). Cell atlas of the human ocular anterior segment: Tissue-specific and shared cell types. *Proc Natl Acad Sci U S A* **119**, e2200914119.

Verdin, E. (2015). NAD(+) in aging, metabolism, and neurodegeneration. *Science* **350**, 1208-13.

Verma, S. S., Gudiseva, H. V., Chavali, V. R. M., Salowe, R. J., Bradford, Y., Guare, L., Lucas, A., Collins, D. W., Vrathasha, V., Nair, R. M. et al. (2024). A multi-cohort genome-wide association study in African ancestry individuals reveals risk loci for primary open-angle glaucoma. *Cell* **187**, 464-480 e10.

Vittal, V., Rose, A., Gregory, K. E., Kelley, M. J. and Acott, T. S. (2005). Changes in gene expression by trabecular meshwork cells in response to mechanical stretching. *Invest Ophthalmol Vis Sci* **46**, 2857-68.

Vollrath, D., Jaramillo-Babb, V. L., Clough, M. V., McIntosh, I., Scott, K. M., Lichter, P. R. and Richards, J. E. (1998). Loss-of-function mutations in the LIM-homeodomain gene, LMX1B, in nail-patella syndrome. *Hum Mol Genet* **7**, 1091-8.

Vranka, J. A., Kelley, M. J., Acott, T. S. and Keller, K. E. (2015). Extracellular matrix in the trabecular meshwork: intraocular pressure regulation and dysregulation in glaucoma. *Exp Eye Res* **133**, 112-25.

Wang, K., Li, G., Read, A. T., Navarro, I., Mitra, A. K., Stamer, W. D., Sulchek, T. and Ethier, C. R. (2018). The relationship between outflow resistance and trabecular meshwork stiffness in mice. *Sci Rep* **8**, 5848.

Weirauch, M. T., Yang, A., Albu, M., Cote, A. G., Montenegro-Montero, A., Drewe, P., Najafabadi, H. S., Lambert, S. A., Mann, I., Cook, K. et al. (2014). Determination and inference of eukaryotic transcription factor sequence specificity. *Cell* **158**, 1431-1443.

Williams, P. A., Harder, J. M., Cardozo, B. H., Foxworth, N. E. and John, S. W. M. (2018). Nicotinamide treatment robustly protects from inherited mouse glaucoma. *Commun Integr Biol* **11**, e1356956.

Williams, P. A., Harder, J. M., Foxworth, N. E., Cardozo, B. H., Cochran, K. E. and John, S. W. M. (2017a). Nicotinamide and WLD(S) Act Together to Prevent Neurodegeneration in Glaucoma. *Front Neurosci* **11**, 232.

Williams, P. A., Harder, J. M., Foxworth, N. E., Cochran, K. E., Philip, V. M., Porciatti, V., Smithies, O. and John, S. W. (2017b). Vitamin B(3) modulates mitochondrial vulnerability and prevents glaucoma in aged mice. *Science* **355**, 756-760.

Xin, Y., Lyu, P., Jiang, J., Zhou, F., Wang, J., Blackshaw, S. and Qian, J. (2022). LRLoop: a method to predict feedback loops in cell-cell communication. *Bioinformatics* **38**, 4117-4126.

Yu, G., Wang, L. G., Han, Y. and He, Q. Y. (2012). clusterProfiler: an R package for comparing biological themes among gene clusters. *OMICS* **16**, 284-7.

Yu, M., Chen, X., Wang, N., Cai, S., Li, N., Qiu, J., Brandt, C. R., Kaufman, P. L. and Liu, X. (2008). H-1152 effects on intraocular pressure and trabecular meshwork morphology of rat eyes. *J Ocul Pharmacol Ther* **24**, 373-9.

Yue, B. Y. (1996). The extracellular matrix and its modulation in the trabecular meshwork. *Surv Ophthalmol* **40**, 379-90.

Zhang, C., Simon, M., Lim, H., Tolman, N. G., Horbal, L., Juarez, F. A., Bhandari, A., Montgomery, C. and John, S. W. M. (2024). IOP-induced blood-retinal barrier compromise contributes to RGC death in glaucoma. *bioRxiv*.

Zhang, M. and Rao, P. V. (2005). Blebbistatin, a novel inhibitor of myosin II ATPase activity, increases aqueous humor outflow facility in perfused enucleated porcine eyes. *Invest Ophthalmol Vis Sci* **46**, 4130-8.

Zhang, Z. Q., Xie, Z., Chen, S. Y. and Zhang, X. (2023). Mitochondrial dysfunction in glaucomatous degeneration. *Int J Ophthalmol* **16**, 811-823.